



HAL
open science

On Planet Formation around Supermassive Black Holes and Grain Disruption Barriers by Radiative Torques

Nguyen Chau Giang, Thiem Hoang, Le Ngoc Tram, Nguyen Duc Dieu, Pham
Ngoc Diep, Nguyen Thi Phuong, Bui Van Tuan, Bao Truong

► **To cite this version:**

Nguyen Chau Giang, Thiem Hoang, Le Ngoc Tram, Nguyen Duc Dieu, Pham Ngoc Diep, et al..
On Planet Formation around Supermassive Black Holes and Grain Disruption Barriers by Radiative
Torques. The Astrophysical Journal, 2022, 936, 10.3847/1538-4357/ac80c2 . insu-03777332

HAL Id: insu-03777332

<https://insu.hal.science/insu-03777332>

Submitted on 15 Sep 2022

HAL is a multi-disciplinary open access archive for the deposit and dissemination of scientific research documents, whether they are published or not. The documents may come from teaching and research institutions in France or abroad, or from public or private research centers.

L'archive ouverte pluridisciplinaire **HAL**, est destinée au dépôt et à la diffusion de documents scientifiques de niveau recherche, publiés ou non, émanant des établissements d'enseignement et de recherche français ou étrangers, des laboratoires publics ou privés.



Distributed under a Creative Commons Attribution 4.0 International License



On Planet Formation around Supermassive Black Holes and Grain Disruption Barriers by Radiative Torques

Nguyen Chau Giang^{1,2}, Thiem Hoang^{1,2}, Le Ngoc Tram³, Nguyen Duc Dieu⁴, Pham Ngoc Diep⁵,
Nguyen Thi Phuong^{1,5}, Bui Van Tuan⁶, and Bao Truong^{1,2,7,8}

¹ Korea Astronomy and Space Science Institute, Daejeon 34055, Republic of Korea; thiemhoang@kasi.re.kr

² Korea University of Science and Technology, Daejeon 34113, Republic of Korea

³ Max Planck Institute for Radio Astronomy, Auf dem Hügel 69, D-53121 Bonn, Germany

⁴ Université de Lyon 1, ENS de Lyon, CNRS, Centre de Recherche Astrophysique de Lyon (CRAL) UMR5574, F-69230 Saint-Genis-Laval, France

⁵ Vietnam National Space Center, Vietnam Academy of Science and Technology, 18 Hoang Quoc Viet, Hanoi, Vietnam

⁶ University of Science and Technology of Hanoi, Vietnam Academy of Science and Technology, 18 Hoang Quoc Viet, Hanoi, Vietnam

⁷ Department of Physics, International University, Ho Chi Minh City, Vietnam

⁸ Vietnam National University, Ho Chi Minh City, Vietnam

Received 2021 November 23; revised 2022 June 24; accepted 2022 July 11; published 2022 September 6

Abstract

It has recently been suggested that planets can form by dust coagulation in the tori of active galactic nuclei (AGN) with low luminosities of $L_{\text{bol}} \lesssim 10^{42} \text{ erg s}^{-1}$, constituting a new class of exoplanets orbiting supermassive black holes called *blanets*. However, large dust grains in the AGN torus may be rotationally disrupted by the radiative torque disruption (RATD) mechanism due to AGN radiation feedback, which would prevent blanet formation. To test this scenario, we adopt a simple smooth and a clumpy dust/gas distribution inside the torus region to study the effect of RATD on the evolution of composite dust grains in the midplane of the torus. We found that grain growth and then blanet formation are possible in the smooth torus model. However, in the clumpy torus model, grain growth will be strongly constrained by RATD, assuming the gas density distribution as adopted by Wada et al. We also found that icy grain mantles inside clumps are quickly detached from the grain cores by rotational desorption, reducing the sticking coefficient between icy grains and the coagulation efficiency. The grain rotational disruption and ice desorption occur on timescales much shorter than the growth time up to a factor of $\sim 10^4$, which are the new barriers that grain growth must overcome to form blanets. Further studies with more realistic AGN models are required to constrain better the effect of RATD on grain growth and blanet formation hypothesis around low-luminosity AGN.

Unified Astronomy Thesaurus concepts: Active galactic nuclei (16); Astrophysical dust processes (99); Interstellar dust (836); Exoplanet formation (492)

1. Introduction

Planets are thought to form from dust grains in the protoplanetary disks (PPDs) around young stars. Although the precise mechanism of planet formation remains elusive, one of the leading theories is *core accretion* which is induced by dust coagulation and gravitational instabilities (Goldreich & Ward 1973; Kokubo & Ida 2012). According to the core accretion theory, small dust grains covered by ice mantles collide and stick together to form large dust aggregates, followed by the formation of planetesimals of kilometer sizes (Kataoka et al. 2013; Okuzumi et al. 2012). Subsequently, gravity acts on planetesimals to form planets (see Chiang et al. 2010 for a review). Recently, Wada et al. (2019) and Wada et al. (2021) studied the possibility of planet formation in the dusty tori around supermassive black holes (SMBHs) and suggested that planets can be formed by coagulation of icy grain mantles beyond the snow line, provided that the luminosities of active galactic nuclei (AGN) are relatively low, around $L_{\text{bol}} \sim 10^{42} \text{ erg s}^{-1}$. Such a proposed scenario is expected to present a new class of exoplanets orbiting SMBHs, termed as *blanets*.

While dust grains in the midplane of PPDs are significantly shielded from stellar radiation due to the high gas density, dust grains in the tori around SMBHs are subject to intense radiation feedback from the AGN. Thus, dust grains can be spun up to extremely fast rotation by radiative torques (RATs) such that the centrifugal force can disrupt micron-sized grains to smaller fragments (Hoang et al. 2019b). This radiative torque disruption (RATD) mechanism is an essential dynamical constraint for the grain size distribution in the interstellar medium (Hoang et al. 2019b), which would be a critical barrier for blanet formation around SMBHs because large aggregates have a lower tensile strength (Tatsumi et al. 2019; Kimura et al. 2020) and will be disrupted more easily than small ones.

The effect of RATD on grain growth and planet formation in PPDs is studied in detail by Tung & Hoang (2020). The authors found that the RATD effect is inefficient in the disk interior thanks to the shielded stellar radiation and very high gas density of $n_{\text{H}} > 10^{10} \text{ cm}^{-3}$. Compared to PPDs, the environment condition for blanet formation around SMBHs is radically different, with a lower gas density of $n_{\text{H}} \sim 10^4 - 10^6 \text{ cm}^{-3}$ at $r = 1 \text{ pc}$ in the midplane of the torus (Wada et al. 2016, 2019, 2021) and an intense radiation field of $L_{\text{bol}} = 10^{42} \text{ erg s}^{-1}$. Recently, Giang & Hoang (2021) studied the influence of RATD on composite grains around a high AGN luminosity of $L_{\text{bol}} = 10^{46} \text{ erg s}^{-1}$. They found that large grains of $a \geq 0.1 \mu\text{m}$ are significantly disrupted to smaller sizes up to distances of $r \sim 100 \text{ pc}$ in the polar cone and $r \sim 10 \text{ pc}$ in

the midplane of the torus. Therefore, it is important to study the strength of RATD around low-luminosity AGN to understand whether RATD suppresses grain growth via coagulation or not.

On the other hand, Wada et al. (2019) studied grain growth beyond the snow line of the torus where ice can form on the surfaces of solid grain cores. The presence of ice mantles increases the sticking collision between icy monomers and reduces fragmentation due to dust collisions (Chokshi et al. 1993; Gundlach et al. 2011). Large icy dust aggregates with highly porous structures thus can grow quickly and overcome the “radial drift barrier” to form planetesimals of kilometer sizes (Okuzumi et al. 2012). However, Hoang & Tram (2020) showed that fast rotating icy grain mantles due to RATs could cause separation between the two components following the fragmentation of detaching ice mantles and then the quick sublimation of icy fragments to the gas phase. This mechanism is named rotational desorption. Considering this effect on PPDs, Tung & Hoang (2020) found the significant removal of micron-sized icy grain mantles beyond the “original” snow line in the dense midplane region. The formation of thick ice mantles is more strongly suppressed due to efficient rotational desorption, where icy dust with size $a \sim 0.5 \mu\text{m}$ only can be formed at the outer boundary of a disk of $r \sim 300 \text{ au}$. Therefore, we expect a similar effect on the evolution of icy grain mantles in the midplane of low-luminosity AGN and rotational desorption may be another barrier that prevents planet formation.

To model the effect of rotational disruption and desorption around low-luminosity AGN, one needs to know in detail the morphology and the distribution of gas and dust grains within the torus region. However, the real geometry of the torus region is still debated. Numerical studies of the circumnuclear region showed that both the smooth torus model, in which the dust and gas distribute smoothly in the flared or tapered geometry of the torus (Fritz et al. 2006; Schartmann et al. 2008), and the clumpy torus model, in which the dust and gas concentrate into dense clumps that distribute randomly inside the diffuse torus region (Nenkova et al. 2002, 2008b; Hönig & Kishimoto 2010), generally can reproduce the observed properties of the spectral energy distribution (SED) in the infrared (IR) range, the feature of the line emission/absorption, and also the broad X-ray spectrum observed from AGN (Buchner et al. 2015). However, high-resolution observations toward circumnuclear regions tend to reveal an inhomogeneous distribution of gas and dust grains instead of a homogeneous or discrete gas/dust distribution as proposed in the smooth and clumpy torus model (Shi et al. 2006; Hicks et al. 2009; Izumi et al. 2018). This picture is consistent with the multi-gas phase structure driven by the radiation-driven fountain model proposed by Wada et al. (2009) (Schartmann et al. 2014; Wada et al. 2016). This model also can reproduce many of the photometric and spectroscopic observations made of AGN (Buchner et al. 2021). However, since the main purpose of our paper is to give the first insight into the effect of rotational disruption and desorption on grain growth around low-luminosity AGN, we adopt the two simple models of the smooth torus model and the clumpy model. We first perform numerical calculations of the disruption size of dust grains with composite structures and the desorption size of icy grain mantles for low-luminosity AGN with $L_{\text{bol}} = 10^{42} \text{ erg s}^{-1}$. Next, we compare the timescale between grain growth via coagulation and rotational destruction and desorption to understand how spinning dust affects grain evolution.

The structure of the paper is as follows. The SED of AGN and the model of the torus are described in Section 2. In Section 3, we briefly describe the mechanism of RATD, the radiative transfer model, and numerical calculations of the grain disruption size by RATD for a smooth and a clumpy gas/dust density model in the torus. We then study the destruction of icy grain mantles beyond the snow line under the effect of rotational desorption in Section 4. We compare the disruption and desorption timescales with the growth time by dust coagulation in Section 5. A discussion of the rotational effect on planet formation around SMBHs is presented in Sections 6, and a summary of our main findings is presented in Section 7.

2. Model of the AGN Radiation Field and Dusty Torus

2.1. SED

We adopt the SED of an unobscured AGN from the studies of Nenkova et al. (2008a) and Stalevski et al. (2012), which follows:

$$\lambda L_{\lambda} = A \begin{cases} 0.158 (\lambda/1 \mu\text{m})^{1.2} & \text{if } 0.001 \leq \lambda \leq 0.01 \mu\text{m} \\ 6.3 \times 10^{-4} & \text{if } 0.01 < \lambda \leq 0.1 \mu\text{m} \\ 2 \times 10^{-4} (\lambda/1 \mu\text{m})^{-0.5} & \text{if } 0.1 < \lambda \leq 5 \mu\text{m} \\ 0.011 (\lambda/1 \mu\text{m})^{-3} & \text{if } 5 < \lambda \leq 50 \mu\text{m} \end{cases}, \quad (1)$$

where A is a normalization constant determined by the bolometric luminosity L_{bol} of AGN. For convenience, we consider that an AGN is a time-invariant source.

In order to model the effect of RATD, we only focus on the main radiation spectrum emitted from the accretion disk from $\lambda_{\text{min}} = 0.1 \mu\text{m}$ to $\lambda_{\text{max}} = 20 \mu\text{m}$ at which the lower limit is determined by the Lyman absorption of neutral hydrogen atoms. To describe the strength of the radiation field, we use the dimensionless parameter $U = u_{\text{rad}}/u_{\text{ISRF}}$ where u_{rad} is the radiation energy density of the local radiation field and $u_{\text{ISRF}} = 8.64 \times 10^{-13} \text{ erg cm}^{-3}$ is the energy density of the average interstellar radiation field (ISRF) in the solar neighborhood (Mathis et al. 1983).

2.2. Physical Model of the AGN Torus

2.2.1. Smooth Torus Model

The right part of Figure 1 shows a two-dimensional illustration of an AGN with a smooth distribution of dust and gas in the torus (hereafter, the smooth torus model). In the dense environment, such as the midplane of the torus region, dust and gas are likely in thermal equilibrium, so that the gas temperature can be inferred from the dust temperature (i.e., $T_{\text{gas}} \approx T_{\text{dust}}$) determined by the balance between grain heating by UV–optical radiation from the central AGN and grain cooling by IR reemission. The equilibrium temperature of large grains of size $a \geq 0.01 \mu\text{m}$ was approximately given by Draine (2011):

$$T_{\text{dust}}(a) \simeq 16.4 U^{1/6} \left(\frac{a}{0.1 \mu\text{m}} \right)^{-1/15} \text{ K}. \quad (2)$$

Dust grains near the center region exposed to higher U have higher temperatures and can be sublimated when the temperature exceeds the sublimation threshold, T_{sub} . The distance where dust starts to survive from thermal sublimation is called

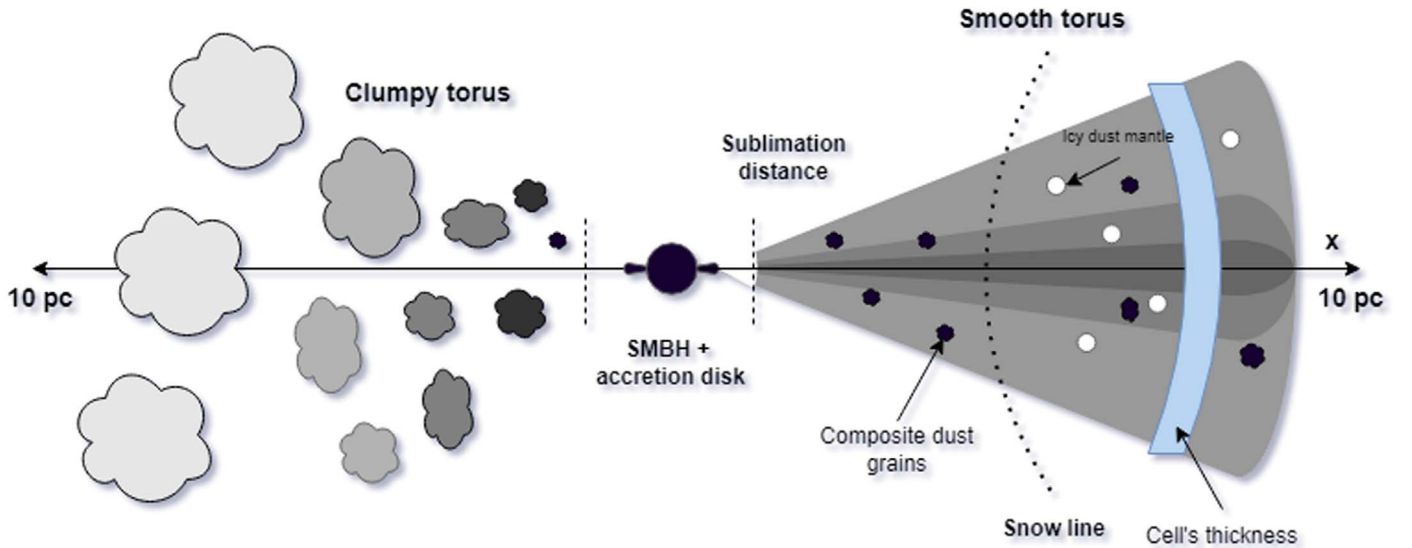


Figure 1. Illustration of an AGN torus in two dimensions with a smooth gas/dust density distribution (e.g., the smooth torus model, right part), and a clumpy gas/dust distribution (the clumpy torus model, left part), around a central SMBH (black circle) and an accretion disk. On the right-hand side, composite dust grains (small black circles) and icy grain mantles (small white circles) are present beyond the sublimation front determined by a dust temperature of $T_{\text{sub}} = 1200$ K and the snow line defined by an ice temperature of 170 K, respectively. On the left-hand side, small, dense clumps (dark clumps) are located near the central region, while large, dilute clumps (light clumps) are located far from the center. To model the effect of dust reddening, we divide the torus (in the case of the smooth torus model) and clumps (in the case of the clumpy torus model) into the equally small spherical shells of thickness d_{cell} (blue cell).

the sublimation distance, denoted as r_{sub} . Here, we assume that carbonaceous grains have the same sublimation temperature of $T_{\text{sub}} = 1200$ K as silicate grains. Therefore, the sublimation distance r_{sub} of grain size a can be found by setting $T_{\text{dust}}(a) = T_{\text{sub}}$, yielding (Draine 2011):

$$r_{\text{sub}} \simeq 2 \times 10^{-3} \text{ pc} \left(\frac{L_{\text{bol}}}{10^{42} \text{ erg s}^{-1}} \right)^{1/2} \left(\frac{T_{\text{sub}}}{1200 \text{ K}} \right)^{-3} \times \left(\frac{a}{0.01 \mu\text{m}} \right)^{-1/5}. \quad (3)$$

We consider the sublimation distance of small grains of $a = 0.01 \mu\text{m}$ as the inner boundary of dusty torus region, which yields $r_{\text{sub}} = 0.002 \text{ pc}$ for $L_{\text{bol}} = 10^{42} \text{ erg s}^{-1}$, assuming $T_{\text{sub}} = 1200$ K.

We assume the simple flared disk geometry for the torus from Fritz et al. (2006) and the gas density profile from Wada et al. (2021) which is given by:

$$n_{\text{H}} = \begin{cases} n_{\text{H},0.05} & \text{for } r < 0.05 \text{ pc} \\ n_{\text{H},1} (r/\text{pc})^{-3/2} & \text{for } r \geq 0.05 \text{ pc} \end{cases}, \quad (4)$$

where $n_{\text{H},0.05}$ and $n_{\text{H},1}$ are the gas density at $r = 0.05 \text{ pc}$ and $r = 1 \text{ pc}$, respectively.

In our study, we only focus on studying the RATD effect on dust in the midplane of the torus where most of the dust is present and planet formation is suggested to occur (Wada et al. 2019).

2.2.2. Clumpy Torus Model

Dust and gas are also suggested to concentrate into dense clumps within the diffuse circumnuclear region (left part of Figure 1). This clumpy torus model was first proposed by Krolik & Begelman (1988) as a way to reduce dust destruction by intense UV–optical AGN radiation. It was then widely studied (e.g., Nenkova et al. 2002, 2008b; Netzer 2015;

Dullemond & van Bemmelen 2005) and supported by observations (e.g., Alonso-Herrero et al. 2016). For this configuration, small and dense clumps (dark color) are likely located near the AGN center, while large and dilute clumps (light color) are located in the middle and outer boundary of the torus (see also the three-dimensional (3D) structure of the clumpy torus model in Schartmann et al. 2008). The variation of the clump size R_{cl} with distance can be assumed as (Höning & Kishimoto 2010):

$$R_{\text{cl}} = \left(\frac{R_{\text{cl},0}}{r_{\text{sub}}} \right) \left(\frac{r}{r_{\text{sub}}} \right)^{\beta_{\text{cl}}} r_{\text{sub}}, \quad (5)$$

where $R_{\text{cl},0}$ is the clump radius at the sublimation front r_{sub} and β_{cl} is the power-law index of the distribution. We assume $R_{\text{cl},0} = 0.01 r_{\text{sub}}$. To simplify the model, we consider that the near side of the clump (closer to the AGN) is directly illuminated by AGN radiation and only consider radiation attenuation inside the clump.

We adopt the same gas density profile as in the smooth torus model given by Equation (4) for comparison. The gas temperature is taken from Equation (2) due to the thermal equilibrium between gas and dust inside the dense clump.

3. Rotational Disruption of Composite Grains

We first describe the main points of the RATD mechanism in Section 3.1 and the radiative transfer modeling in Section 3.2. The numerical calculations of the disruption size of composite grains for the smooth and clumpy torus models are described in Section 3.3.

3.1. RATD Mechanism

Following the principle of RATD (Hoang et al. 2019b), a fast rotating irregular dust grain spun up by RATs (Draine & Weingartner 1996; Lazarian & Hoang 2007) can be destroyed to smaller pieces if the induced tensile stress exceeds the maximum tensile strength of the dust grain. Assuming a

constant AGN radiation field, the time evolution of the grain's angular velocity driven by RATs is given by:

$$\omega(t) = \omega_{\text{RAT}}(1 - e^{-t/\tau_{\text{damp}}}), \quad (6)$$

where τ_{damp} is the gas damping timescale, which is:

$$\tau_{\text{damp}} = \frac{\tau_{\text{gas}}}{1 + \text{FIR}}, \quad (7)$$

where τ_{gas} is the typical timescale for the rotational damping by gas collisions and FIR is the coefficient representing the rotational damping caused by IR reemission (see Hoang et al. 2019b for details). ω_{RAT} is the maximum angular velocity that the dust grain can reach after a long time. For an irregular grain of effective size a which is defined as the radius of a spherical grain with the same volume, the formula for ω_{RAT} is described by Hoang et al. (2019b) and Giang & Hoang (2021):

$$\omega_{\text{RAT}} \approx 1.2 \times 10^{11} \gamma_{\text{rad}} a_{-5}^{0.7} \bar{\lambda}_{0.5}^{-1.7} \times \left(\frac{U_6}{1.2n_5 T_2^{1/2}} \right) \left(\frac{1}{1 + F_{\text{IR}}} \right) \text{rad s}^{-1}, \quad (8)$$

for a grain of size $a \leq \bar{\lambda}/1.8$, and

$$\omega_{\text{RAT}} \approx 2.1 \times 10^{12} \gamma_{\text{rad}} a_{-5}^{-2} \bar{\lambda}_{0.5} \times \left(\frac{U_6}{1.2n_5 T_2^{1/2}} \right) \left(\frac{1}{1 + F_{\text{IR}}} \right) \text{rad s}^{-1}, \quad (9)$$

for a grain of size $a > \bar{\lambda}/1.8$. In these equations, $a_{-5} = a/(10^{-5} \text{ cm})$, $\bar{\lambda}_{0.5} = \bar{\lambda}/(0.5 \mu\text{m})$, with $\bar{\lambda}$ the mean wavelength of the radiation spectrum from $\lambda = 0.1 - 20 \mu\text{m}$, $U_6 = U/(10^6)$ is the radiation strength, $n_5 = n_{\text{H}}/(10^5 \text{ cm}^{-3})$, and $T_2 = T_{\text{gas}}/(100 \text{ K})$ is the gas temperature given by Equation (2). Also, γ_{rad} is the anisotropic degree of the radiation field ($0 \leq \gamma_{\text{rad}} \leq 1$), and we adopt $\gamma_{\text{rad}} = 1$ for the unidirectional radiation field of AGN. The last term of F_{IR} is the dimensionless coefficient of rotational damping due to thermal dust emission (see Hoang et al. 2019b for details). The change of ω_{RAT} at $a = a_{\text{trans}} = \bar{\lambda}/1.8$ is due to a change of the RAT efficiency with the mean wavelength $\bar{\lambda}$ and grain size a (see Hoang & Lazarian 2008, 2014; Hoang et al. 2019b; Giang & Hoang 2021 for details).

The rotating dust grain will be disrupted to smaller sizes if its tensile stress, $S = \rho a^2 \omega^2/4$, exceeds the maximum tensile strength of the grain material, S_{max} . The value of S_{max} depends on the grain material, grain structure, and grain size, which have not yet well constrained. An ideal material can have a high maximum tensile strength, such as a diamond with $S_{\text{max}} \sim 10^{11} \text{ erg cm}^{-3}$ (Draine & Salpeter 1979; Burke & Silk 1974), or a polycrystalline bulk material with $S_{\text{max}} \sim 10^9 - 10^{10} \text{ erg cm}^{-3}$ (Hoang et al. 2019b), while composite dust grains which are formed via sticking collisions between submicron grains in cold and dense environments such as molecular clouds and PPDs (Tatsumura et al. 2019; Kimura et al. 2020) are expected to be porous with a low maximum tensile strength of $S_{\text{max}} \sim 10^5 - 10^8 \text{ erg cm}^{-3}$ (Hoang 2019).

The critical angular velocity for rotational disruption can be found by setting the centrifugal stress $S = S_{\text{max}}$, which is

given by:

$$\omega_{\text{disr}} = \frac{2}{a} \left(\frac{S_{\text{max}}}{\rho} \right)^{1/2} = \frac{1.14 \times 10^9}{a_{-5}} S_{\text{max},8}^{1/2} \hat{\rho}^{-1/2} \text{ rad s}^{-1}, \quad (10)$$

where $S_{\text{max},8} = S_{\text{max}}/(10^8 \text{ erg cm}^{-3})$ and $\hat{\rho} = \rho/(3 \text{ g cm}^{-3})$ with ρ the grain mass density. The disruption threshold decreases with decreasing maximum tensile strength and increasing grain size, implying the strong effect of RATD on large composite grains.

Comparing Equation (8) with Equation (10) for grains of $a \leq a_{\text{trans}}$, one can see that large grains are more easily destroyed by RATD due to an increase of ω_{RAT} and a decrease of ω_{disr} with increasing grain size. The first intersection between ω_{RAT} and ω_{disr} determines the grain disruption size, denoted by a_{disr} , above which dust will be disrupted by RATD. By comparing Equation (9) with Equation (10) for grains of $a > a_{\text{trans}}$, it is harder for grains with larger sizes to be destroyed due to a decrease of ω_{RAT} with increasing grain size. Thus, the second intersection between ω_{RAT} and ω_{disr} determines the maximum size that dust will still be affected by RATD, denoted by $a_{\text{disr,max}}$. The range of disrupted grains of $a_{\text{disr}} - a_{\text{disr,max}}$ will be extended for a stronger radiation field and a weaker maximum tensile strength S_{max} .

3.2. Radiative Transfer Model

UV-optical radiation passing through the dusty torus will be attenuated due to scattering and absorption by dust grains. The spectral energy density at distance r from the central source thus will be given by:

$$u_{\lambda} = u_{\lambda,0} e^{-\tau_{\lambda}}, \quad (11)$$

where $u_{\lambda,0} = L_{\lambda,0}/(4\pi cr^2)$ is the intrinsic energy density, with $L_{\lambda,0}$ the specific luminosity given by Equation (1), and τ_{λ} is the optical depth at wavelength λ .

We adopt the popular interstellar dust model consisting of separate astronomical silicate and carbonaceous grains (see Li & Draine 2001; Weingartner & Draine 2001; Draine & Li 2007) where the grain size spans from a minimum size of $a_{\text{min}} = 3.5 \text{ \AA}$ to a maximum size of $a_{\text{max}} = 10 \mu\text{m}$. We assume that dust grains initially follow the Mathis–Rumpl–Nordseick (MRN) distribution of $dn/da = n_{\text{H}} C a^{-3.5}$ (Mathis et al. 1977) with C the normalization constant determined by the dust-to-gas mass ratio η (Laor & Draine 1993). We consider the presence of micron-sized grains in the torus, thus, in order to keep the typical dust-to-gas mass ratio found in the interstellar medium to $\eta = 0.01$, the normalization constant must be reduced by a factor of 3 from the values of Mathis et al. (1977), to $C_{\text{sil}} = 1.16 \times 10^{-26} \text{ cm}^{2.5}$ and $C_{\text{carb}} = 1.036 \times 10^{-26} \text{ cm}^{2.5}$, respectively.

Without RATD, AGN radiation is attenuated by all grains from a_{min} to a_{max} . With RATD, grains of size from a_{disr} to $a_{\text{disr,max}}$ are disrupted to smaller sizes, resulting in two separate populations of the grain size distribution. The first population includes grains of size from a_{min} to a_{disr} , which are enhanced by the disruption of large grains by RATD. The second population includes large grains from $a_{\text{disr,max}}$ to a_{max} which are not affected by RATD and still follow the MRN distribution. Due to a lack of information about the redistribution of

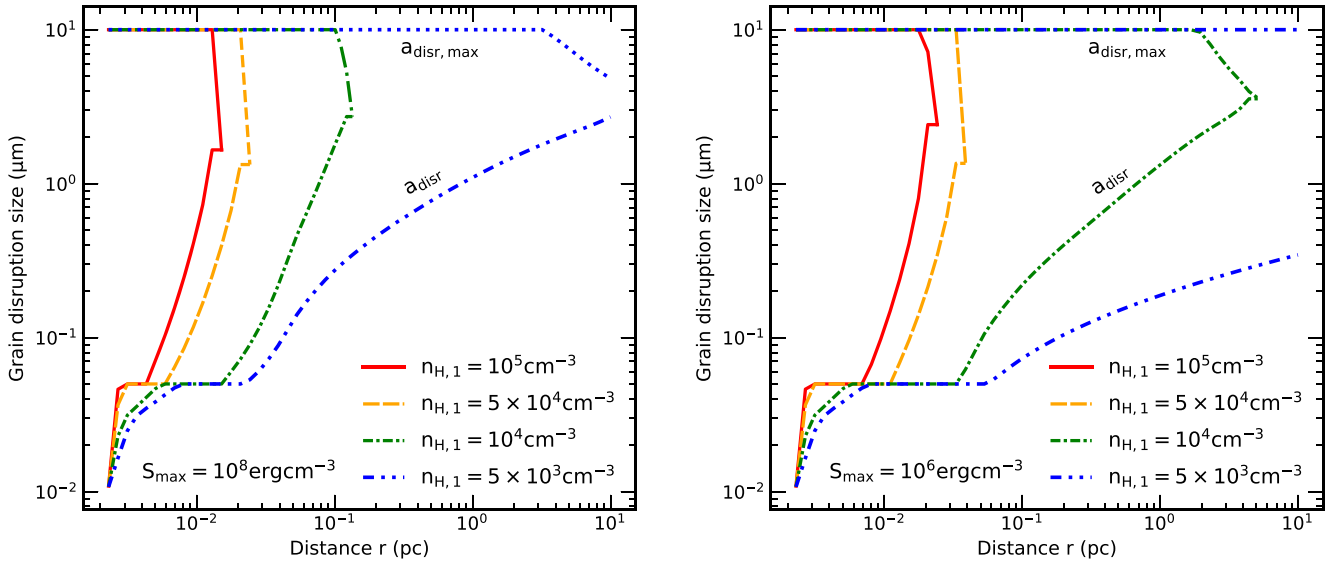


Figure 2. Dependence of the range of the disruption sizes of composite grains, $a_{\text{disr}} - a_{\text{disr,max}}$, on the distance to the AGN center for the smooth torus model, assuming different gas density profiles described by $n_{\text{H},1}$. Two values of $S_{\text{max}} = 10^8 \text{ erg cm}^{-3}$ (typical for compact dust grains) and $S_{\text{max}} = 10^6 \text{ erg cm}^{-3}$ (typical for porous dust grains) are considered in the left and right panels, respectively.

disrupted grains, we assume that small grains of size between $a_{\text{min}} - a_{\text{disr}}$ still follow a power-law distribution with a steeper slope, denoted as ϵ , implying the enhancement of very small grains. Assuming the constant values of C_{sil} and C_{carb} , the new slope ϵ can be found from the mass conservation of dust from a_{min} to $a_{\text{disr,max}}$ (see Giang & Hoang 2021 for details). Consequently, the optical depth at wavelength λ produced by all dust grains from the sublimation front to distance d from the AGN center is given by:

$$\begin{aligned} \tau_{\lambda}(d) &= \sum_{j=\text{sil,carb}} \int_0^d \int C_{\text{ext}}^j(a, \lambda) \frac{dn^j}{da}(r) da \\ &= \sum_{j=\text{sil,carb}} \int_0^d \left(\int_{a_{\text{min}}}^{a_{\text{disr}}(r)} C_{\text{ext}}^j(a, \lambda) a^{\epsilon(r)} da \right. \\ &\quad \left. + \int_{a_{\text{disr,max}}(r)}^{a_{\text{max}}} C_{\text{ext}}^j(a, \lambda) a^{-3.5} da \right) n_{\text{H}}(r) C^j dr, \quad (12) \end{aligned}$$

where $a_{\text{disr}}(r)$, $a_{\text{disr,max}}(r)$, $\epsilon(r)$, and $n_{\text{H}}(r)$ are the grain disruption size, maximum grain disruption size, new power-index of the distribution of grain size of $a \leq a_{\text{disr}}(r)$, and the gas density at distance r given by Equation (4), respectively. Above, $C_{\text{ext}}(a, \lambda) = Q_{\text{ext}}(a, \lambda) \pi a^2$ is the extinction cross section of grain size a with wavelength λ , with $Q_{\text{ext}}(a, \lambda)$ the extinction efficiency. The values of $Q_{\text{ext}}(a, \lambda)$ are adopted from Hoang et al. (2013) for submicron-sized grains and calculated from the public Discrete Dipole Scattering code (DDSCAT; Draine et al. 1994) for micron-sized grains (Giang & Hoang 2021), assuming an oblate spheroidal shape with an axial ratio of 2.

Wada et al. (2019) suggested that micron-sized grains beyond the snow line can grow and form blanets in the midplane of the torus region around low-luminosity AGN. Therefore, we focus to study the effect of RATD and rotational desorption in this region, and consider the radiative transfer of AGN radiation in one dimension, i.e., along the x -direction (Figure 1).⁹

⁹ This choice neglects the angle-dependence of the UV-optical radiation emitted from the accretion disk around AGN.

To numerically model the attenuation of AGN radiation by dust along the x -direction, we divide the midplane of the flared disk (in case of the smooth torus model) and the clumps (in case of the clumpy torus model) into n thin cells of the same thickness $d_{\text{cell}} = 0.01 \text{ pc}$, respectively. The dust size distribution is considered uniform in each cell (see the thin blue cell in Figure 1). The total optical depth produced by dust from the sublimation front to distance d (in the case of the smooth torus model) can be written as:

$$\tau_{\lambda,n} = \sum_{i=1}^n \Delta\tau_{\lambda,i}, \quad (13)$$

where $\Delta\tau_{\lambda,i}$ is the optical depth produced by dust in the i^{th} cell (by using Equation (12) with d replaced by d_{cell}) and i is the order of the cell. We denote $i=1$ as the first cell at the sublimation front and $i=n$ as the last cell at distance d in the x -direction. In the case of the clumpy torus model, $i=1$ is the first cell at the near side (closer to the AGN) of the clump, and $i=n$ is the last cell at distance d from the near side.

3.3. Grain Disruption Size

To study the effect of RATD on composite dust grains in the midplane of torus, we first solve the radiative transfer equation (Equation (11)) to get the radiation strength U with distance, then calculate the terminal angular velocity ω_{RAT} of all grain sizes from a_{min} to a_{max} (Equations (8) and (9)). By comparing ω_{RAT} with the critical angular velocity ω_{disr} (Equation (10)), we can determine the range $a_{\text{disr}} - a_{\text{disr,max}}$ in which grains are destroyed by RATD. We consider the evolution of dust grains under the RATD effect for the typical case of a luminosity of $L_{\text{bol}} = 10^{42} \text{ erg s}^{-1}$ in which a blanet is suggested to form (Wada et al. 2019, 2021).

3.3.1. Smooth Torus Model

The left panel of Figure 2 shows the variation of the disruption size of composite dust grains as a function of distance, assuming different gas density profiles with $n_{\text{H},1}$ varying from $5 \times 10^3 \text{ cm}^{-3}$ to 10^5 cm^{-3} . To account for the

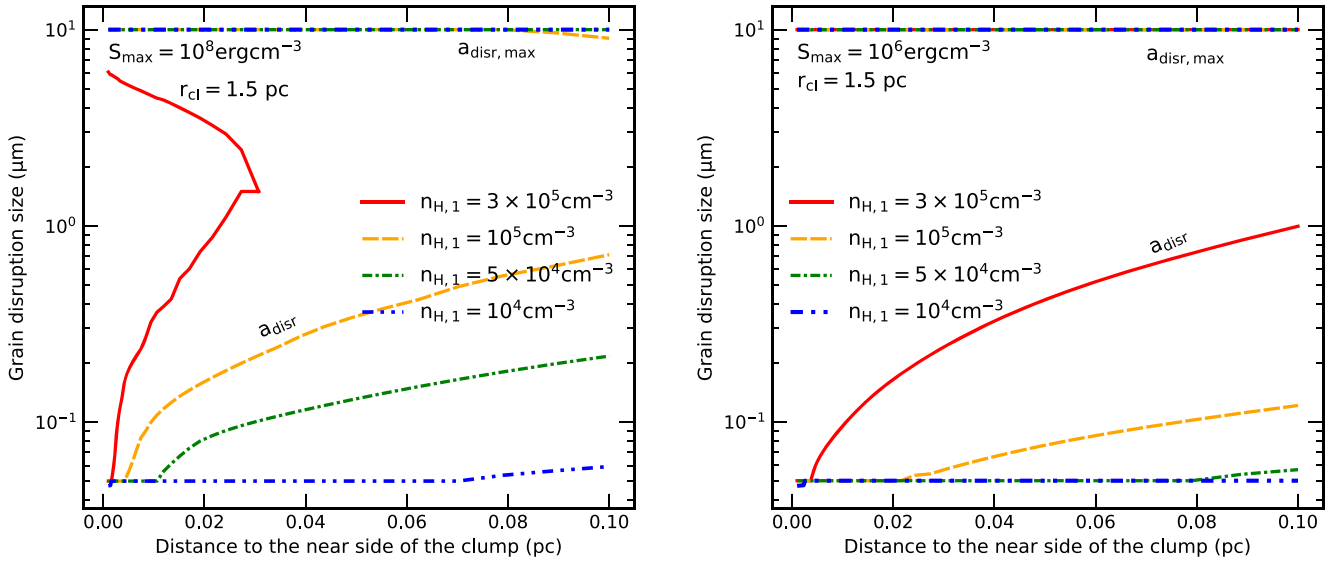


Figure 3. Similar to Figure 2 but for composite grains inside clumps of radius $R_{cl} = 0.05$ pc at $r = 1.5$ pc. The RATD effect is more effective, as demonstrated by a broader range of disruption sizes, due to a reduction of dust reddening (see the main text).

dependence of the maximum tensile strength on the grain size, we adopt $S_{max} = 10^{10}$ erg cm $^{-3}$ for small grains of size $a < 0.05$ μm and $S_{max} = 10^8$ erg cm $^{-3}$ for larger grains. Dust grains are strongly disrupted near the sublimation front due to strong radiation and are less affected by RATD at larger distances, as illustrated by the rise of a_{disr} and the decline of $a_{disr,max}$. The intersection between a_{disr} and $a_{disr,max}$ determines the distance where RATD ceases. We call this boundary the active region of RATD. The disruption of composite dust grains is stronger for lower gas densities due to smaller rotational damping and dust reddening effect. For example, micron-sized grains of $a > 1$ μm can be disrupted by RATD up to $r = 1$ pc if the gas density at $r = 1$ pc decreases below $n_{H,1} \leq 5 \times 10^3$ cm $^{-3}$.

The right panel of Figure 2 shows similar results as the left panel, but assuming large grains of $a > 0.05$ μm and $S_{max} = 10^6$ erg cm $^{-3}$. By decreasing the maximum tensile strength, large grains are more easily destroyed by RATD due to a lower disruption threshold (Equation (10)), resulting in the expansion of the active region of RATD. For example, with a low gas density of $n_{H,1} = 5 \times 10^3$ cm $^{-3}$, all large grains of $a > 0.03$ μm with $S_{max} = 10^6$ erg cm $^{-3}$ can be destroyed by RATD up to the outer boundary of torus at $r = 10$ pc. However, for low-luminosity AGN of $L_{bol} = 10^{42}$ erg s $^{-1}$ with the sublimation distance at $r_{sub} = 0.002$ pc, the smooth distribution of dust density in the torus region produces a very high dust reddening effect that significantly suppresses the RATD effect at the parsec scale. Dust grains at this distance are not affected by rotational disruption if $n_{H,1} > 5 \times 10^3$ cm $^{-3}$.

3.3.2. Clumpy Torus Model

The left panel of Figure 3 shows the variation of grain disruption size with the distance to the near side of the clump (i.e., closest to the AGN) for a clump of radius $R_{cl} = 0.05$ pc located at distance $r = 1.5$ pc, assuming different values of $n_{H,1}$ and $S_{max} = 10^8$ erg cm $^{-3}$. Dust is destroyed stronger toward the near side, while weaker in the middle and far side of the clump. In contrast to the inefficient RATD at the parsec scale in the smooth torus model (see Figure 2), this mechanism now is strong enough to destroy all large grains of $a \geq 1$ μm in a

whole clump located at $r = 1.5$ pc with $n_H < 3 \times 10^5$ cm $^{-3}$. The higher efficiency of RATD comes from the configuration of the clumpy torus model such that dust near the front face of the clump is directly illuminated by strong UV–optical AGN radiation and thus can be destroyed by RATD stronger. However, for a higher gas density of $n_{H,1} > 3 \times 10^5$ cm $^{-3}$, RATD is only efficient to disrupt large grains in the first half of the clumps near the AGN.

The right panel of Figure 3 shows similar results as the left one but for $S_{max} = 10^6$ erg cm $^{-3}$. The RATD effect becomes stronger (i.e., smaller a_{disr}) due to the smaller S_{max} . For instance, micron-sized grains of $a > 0.1$ μm with low $S_{max} = 10^6$ erg cm $^{-3}$ will be totally removed by RATD even if the clumps at $r = 1.5$ pc are optically thick with $n_{H,1} > 3 \times 10^5$ cm $^{-3}$.

We now study the effect of RATD for a given clump of $R_{cl} = 0.1$ pc, assuming a different radiation strength (U_0) and density (n_H) at the near side of the clump. The results for $S_{max} = 10^8$ erg cm $^{-3}$ and $S_{max} = 10^6$ erg cm $^{-3}$ are shown in the left and right panels of Figure 4, respectively. The color from yellow to blue indicates the total disruption of large grains by RATD inside the clump (e.g., the right panel of Figure 3), while the dark blue indicates disruption in the front half of the clump (e.g., the curve with $n_H = 3 \times 10^5$ cm $^{-3}$ in the left panel of Figure 3). The black (e.g., $a_{disr} = a_{max} = 10$ μm) indicates no disruption effect.

For compact grains with $S_{max} = 10^8$ erg cm $^{-3}$ (left panel), they will be efficiently destroyed by RATD in a region with a strong radiation field and/or low gas density (yellow region) and are less affected by RATD in a weak radiation field and/or high density region (dark blue and black region). The constrains of the maximum grain size by RATD is stronger, i.e., smaller a_{disr} , for grains with a lower maximum tensile strength (right panel for grains with $S_{max} = 10^5$ erg cm $^{-3}$). For example, with $U_0 = 10^5$ and $n_H = 10^5$ cm $^{-3}$, RATD only can remove large grains with $S_{max} = 10^8$ erg cm $^{-3}$ in the front half of a clump of size 0.1 pc (dark blue region), while it can destroy all grains larger than 1 μm in the entire clump if grains have $S_{max} = 10^6$ erg cm $^{-3}$.

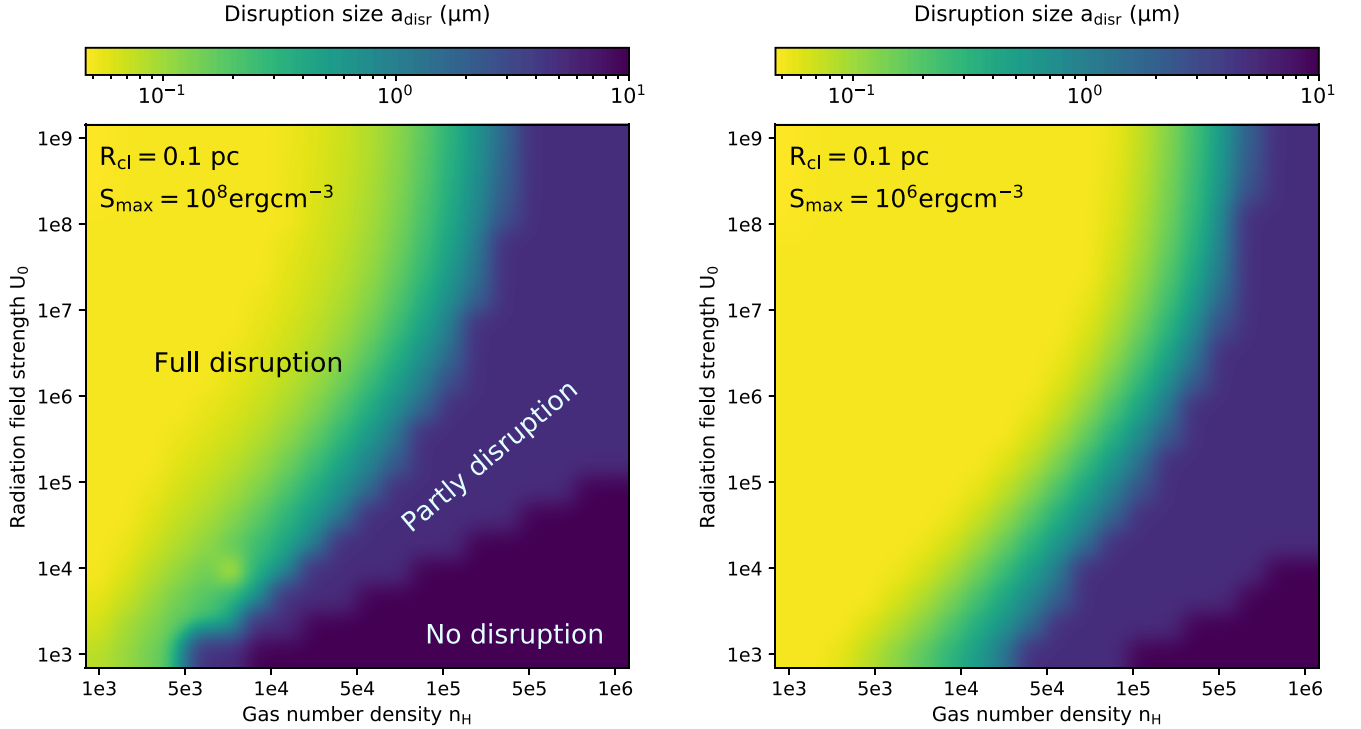


Figure 4. Variation of the grain disruption size at the far side of the clumps as a function of radiation field strength and gas density at the near side of the clumps U_0 and n_H for a clump of size $R_{cl} = 0.1$ pc, assuming $S_{max} = 10^8 \text{ erg cm}^{-3}$ (left panel) and $S_{max} = 10^6 \text{ erg cm}^{-3}$ (right panel). Yellow to blue implies the full dust disruption effect by RATD in clumps and dark blue and black imply the part disruption and no disruption cases.

The upper left panel of Figure 5 shows the variation of gas densities given by Equation (4) and cloud sizes given by Equation (5) with $\beta_{cl} = 0.8$ as a function of distance r (or radiation field strength U). From the $R_{cl} - r$ relation (black line), we sample 35 points from $r - r_{sub}$ to $r - 20$ pc to study the effect of RATD inside clumps. The blue, red, and orange colors present different gas density profiles for a gas density at 1 pc of $n_{H,1} = 10^4$, 10^5 , and $3 \times 10^5 \text{ cm}^{-3}$, respectively. Small, dark circles represent small, dense clumps near the center region while large, faint clumps represent large, optically thin clumps near the outer region (see the left part of Figure 1).

The upper right and lower left panels of Figure 5 show similar disruption size maps as functions of U_0 and n_H as in Figure 4, but account for variations of clump size with distance from the upper left panel. RATD is more efficient in destroying composite dust grains inside the dense and compact clumps near the center region, but less efficient in the dilute and large clumps far from the center. Putting the sample of studied cases (red, blue, and orange circles) from the upper left panel into the map, one can see that with a low gas density of $n_{H,1} = 10^4 \text{ cm}^{-3}$, RATD is efficient enough to suppress the presence of large grains of $a \geq 0.1 \mu\text{m}$ inside the torus. For a higher gas density of $n_H = 3 \times 10^5 \text{ cm}^{-3}$, grains of $a \geq 0.1 \mu\text{m}$ with $S_{max} = 10^8 \text{ erg cm}^{-3}$ at the far side of clumps can survive against RATD and grow to micron sizes. However, the growth of micron-sized grains is likely coupled with a reduction of the material's strength (Dominik & Tielens 1997; Wada et al. 2008; Suyama et al. 2012). For newly formed large grains with $S_{max} = 10^6 \text{ erg cm}^{-3}$ (the lower left panel), they will be quickly disrupted again to smaller sizes. In other words, the maximum grain size inside clumps will be constrained by the strength of RATD.

If clumps inside the torus are bigger and denser than our considered case, dust aggregates have more chance for growing around AGN. This sets the boundary region of RATD that should be taken into account when studying the formation of large grains inside the dusty torus.

4. Rotational Desorption of Icy Grain Mantles

In this section, we study the evolution of icy grain mantles beyond the snow line under the effect of rotational desorption (Hoang & Tram 2020). The rotational desorption mechanism is described in Section 4.1 and the results are shown in Section 4.2.

4.1. Rotational Desorption Mechanism

Similar to rotational disruption of composite dust grains in the intense radiation field described in Section 3.3, an ice mantle can be separated from a solid grain core if the tensile stress produced by the spinning icy grain exceeds the adhesive energy that holds the mantle and the core together (Hoang & Tram 2020).

Let a_c be the effective radius of a spherical grain that has the same volume as the irregular compact grain core and Δa_m is the average thickness of the ice mantle. The effective radius of the icy grain can be considered as $a = a_c + \Delta a_m$. The average tensile stress S produced by the centrifugal force of all ice layers applying on the interface of core mantle is (Hoang & Tram 2020):

$$S = \frac{\rho_{ice} \omega^2 a^2}{4} \left[1 - \left(\frac{a_c}{a} \right)^2 \right], \quad (14)$$

where $\rho_{ice} = 1 \text{ g cm}^{-3}$ is the mass density of ice.

The detachment of the ice mantle from the grain surface will occur when S exceeds the adhesive energy of the mantle. The

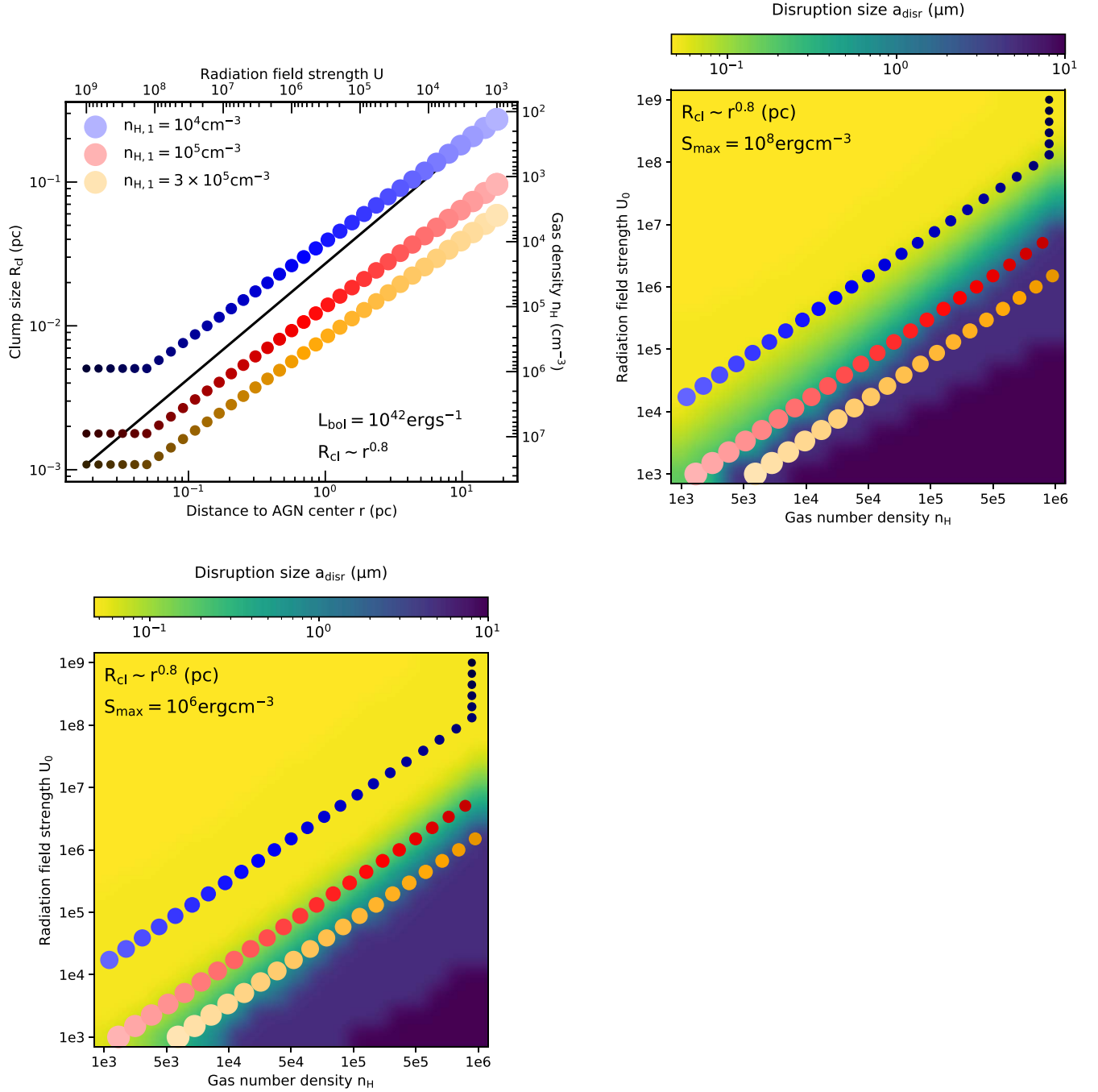


Figure 5. Upper left panel: space dependence of the gas density and clump size as a function of distance r (or radiation field strength U). From the $R_{\text{cl}}-r$ relation (black line), we sample 35 points to study the effect of RATD inside clumps, in which small, dark circles represent small, dense clumps near the center region while large, faint circles represent large, optically thin clumps near the outer region of the torus. We note that each point corresponds to one couple value of $r - n_{\text{H}}$ (horizontal and right vertical axis), and the point size only represents quantitatively the clump size. The upper right and lower left panels: Variation of disruption size at the far side of clumps as functions of U_0 and n_{H} , accounting for the variation of clump size with distance as in the upper left panel. Studied cases are plotted to see how RATD destroys composite dust grains under these conditions.

adhesive energy depends on the surface properties of the solid core, i.e., rough surfaces induce larger adhesive strength up to $\sim 10^9 \text{ erg cm}^{-3}$ (Work & Lian 2018) while smoother surfaces induce lower values. The tensile strength of ice $S_{\text{max,ice}}$ depends on the temperature, where higher temperatures, i.e., 200–300 K, induce a lower value of $S_{\text{max,ice}} \sim 5 \times 10^6 \text{ erg cm}^{-3}$ (Litwin et al. 2012). In this paper, we consider that the adhesive strength has the same value as the maximum tensile strength of ice mantles.

The critical angular velocity for rotational desorption of the ice mantle can be obtained by setting $S = S_{\text{max,ice}}$ (Hoang & Tram 2020), which follows:

$$\begin{aligned} \omega_{\text{desp}} &= \frac{2}{a(1 - a_c^2/a^2)^{1/2}} \left(\frac{S_{\text{max}}}{\rho_{\text{ice}}} \right)^{1/2} \\ &\approx \frac{6.3 \times 10^8 \rho_{\text{ice}}^{-1/2}}{a_{-5}(1 - a_c^2/a^2)^{1/2}} S_{\text{max,ice,7}}^{1/2} \text{ rad s}^{-1}, \end{aligned} \quad (15)$$

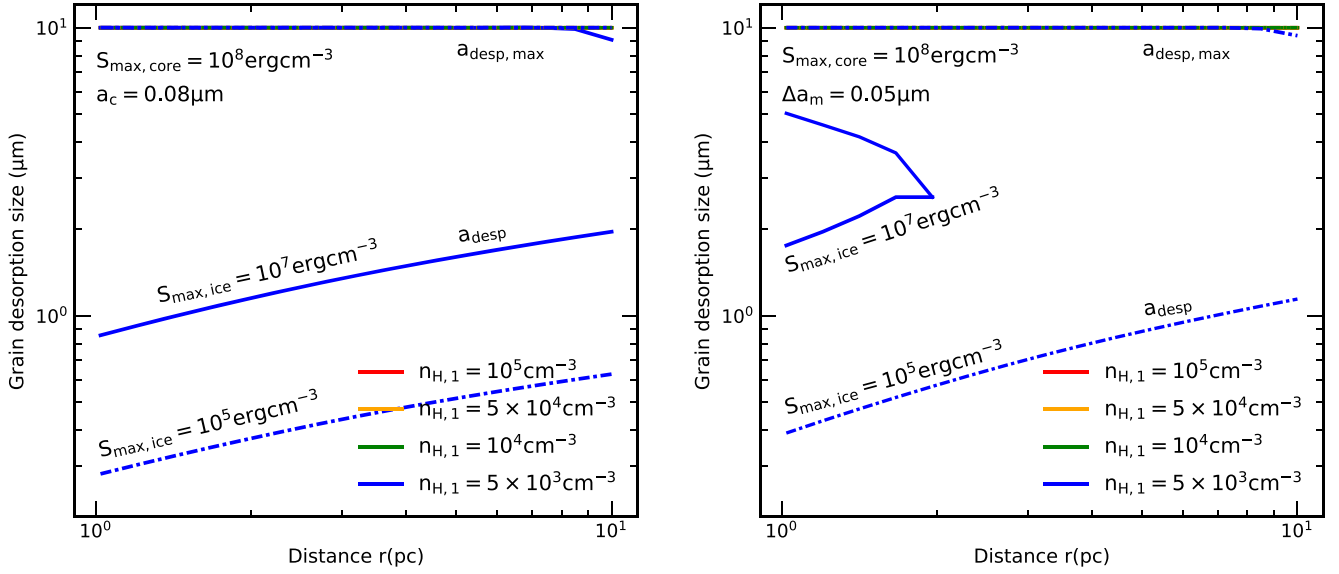


Figure 6. Dependence of the range of the desorption size of the icy grain mantles, $a_{\text{desp}} - a_{\text{desp,max}}$, on the distance to the AGN center for the smooth torus model. Different gas density profiles $n_{\text{H},1}$ and two values of the tensile strengths of ice $S_{\text{max,ice}} = 10^7 \text{ erg cm}^{-3}$ (solid lines) and $S_{\text{max,ice}} = 10^5 \text{ erg cm}^{-3}$ (dashed–dotted lines) are assumed. For high gas density of $n_{\text{H},1} \leq 5 \times 10^3 \text{ cm}^{-3}$ (green, orange, and red lines), ice mantles are not desorbed from the solid core due to the inefficient rotational desorption by a weak radiation field, giving $a_{\text{desp}} = a_{\text{desp,max}} = 10 \mu\text{m}$, i.e., horizontal line at $10 \mu\text{m}$. Rotational desorption of the ice mantles occurs only for $n_{\text{H},1} \leq 5 \times 10^3 \text{ cm}^{-3}$. The left panel is for grain mantles with a fixed grain core of $a_c = 0.08 \mu\text{m}$, while the right panel is for a fixed ice mantle thickness of $\Delta a_m = 0.05 \mu\text{m}$. The grain cores are assumed to have $S_{\text{max}} = 10^8 \text{ erg cm}^{-3}$.

where $S_{\text{max,ice},7} = S_{\text{max,ice}} / (10^7 \text{ erg cm}^{-3})$.

By comparing the maximum angular velocity induced by RATs, ω_{RAT} , for all grain sizes (Equations (8) and (9)) with ω_{desp} , one can determine the range of desorption size $a_{\text{desp}} - a_{\text{desp,max}}$ in which the ice mantle is separated from the grain core.

4.2. Grain Desorption Size

Our numerical calculations of the gas temperature (see Equation (2)) show that ice can exist on composite dust grains beyond $r \sim 1 \text{ pc}$. We will next study the evolution of icy grains under the rotational desorption effect, assuming that the grain core has $S_{\text{max}} = 10^8 \text{ erg cm}^{-3}$.

4.2.1. Smooth Torus Model

The left panel of Figure 6 shows the dependence of the grain desorption size of the icy grain mantles with a fixed grain core of $a_c = 0.08 \mu\text{m}$ on distance, assuming different gas density profiles. The maximum tensile strength of the ice mantles is $S_{\text{max,ice}} = 10^7 \text{ erg cm}^{-3}$ (thick lines) and $S_{\text{max,ice}} = 10^5 \text{ erg cm}^{-3}$ (thin lines). One can see the overlap between a_{desp} and $a_{\text{desp,max}}$ at $a_{\text{max}} = 10 \mu\text{m}$ beyond $r \geq 1 \text{ pc}$ for $n_{\text{H},1} > 10^4 \text{ cm}^{-3}$, indicating no effect of rotational desorption at the parsec scale of the torus region. Ice mantles are only detached from the grain cores only if the gas density at 1 pc declines below $n_{\text{H},1} \leq 5 \times 10^3 \text{ cm}^{-3}$.

The right panel of Figure 6 shows the space-varying desorption size for icy dust with a fixed thickness of the ice mantles of $\Delta a_m = 0.05 \mu\text{m}$. Similar to the left panel, rotational desorption only can affect icy grains at the parsec scale if $n_{\text{H},1} \leq 5 \times 10^3 \text{ cm}^{-3}$. Desorption happens stronger for lower tensile strengths of the ice mantles. In addition, one can see that it is hard for thin ice mantles to be detached from the core, i.e., higher a_{desp} and lower $a_{\text{desp,max}}$, which is attributed to the lower tensile stress in the contact region between the solid core and the ice mantle (see Equation (14)).

4.2.2. Clumpy Torus Model

The upper panel of Figure 7 shows the variation of $a_{\text{desp}} - a_{\text{desp,max}}$ within clumps of radius $R_{\text{cl}} = 0.05 \text{ pc}$ at $r = 1.5 \text{ pc}$ with different gas density profiles, assuming a fixed grain core of $a_c = 0.08 \mu\text{m}$ and $S_{\text{max,ice}} = 10^7 \text{ erg cm}^{-3}$. Icy grain mantles are desorbed stronger near the front side of the clumps and weaker in the middle and back side. Interestingly, one can see that rotational desorption now can affect the icy grain mantles at the parsec scale of the torus region thanks to the direct illumination of UV–optical photons from the center region. The detachment happens stronger for clumps with a lower gas density (i.e., lower $n_{\text{H},1}$). For instance, at the far side of the clumps, the desorption size decreases from $10 \mu\text{m}$ (no rotation desorption effect) for $n_{\text{H},1} = 3 \times 10^5 \text{ cm}^{-3}$ to $a_{\text{desp}} \sim 0.6 \mu\text{m}$ and $0.09 \mu\text{m}$ for $n_{\text{H},1} = 10^5 \text{ cm}^{-3}$ and 10^4 cm^{-3} , respectively.

The lower panel of Figure 7 shows similar results as the upper panel, but for $S_{\text{max,ice}} = 10^5 \text{ erg cm}^{-3}$. For a lower maximum tensile strength of the ice mantles, i.e., a smaller desorption threshold, rotational desorption can detach all icy grains with sizes greater than $1 \mu\text{m}$ even in the dense clumps with $n_{\text{H},1} = 3 \times 10^5 \text{ cm}^{-3}$ at 1.5 pc.

Figure 8 shows the variation of grain desorption size inside clumps of $R_{\text{cl}} = 0.05 \text{ pc}$ located at 1.5 pc for the different gas density profiles, assuming a fixed thickness of the ice mantles of $\Delta a_m = 0.05 \mu\text{m}$. Similar to the case of fixed grain cores, the ice mantles can be detached from the core due to the rotational desorption effect. The detachment is stronger for dilute clumps and ice mantles with a porous structure. However, the thin ice mantles are less separated from the cores due to the lower induced tensile stress at the contact region, i.e., higher a_{desp} compared with the results in Figure 7. For example, with $S_{\text{max,ice}} = 10^7 \text{ erg cm}^{-3}$, ice mantles with thickness $\Delta a_m = 0.05 \mu\text{m}$ never be desorbed from the cores in dense clumps with $n_{\text{H},1} \geq 10^5 \text{ cm}^{-3}$.

The upper panels of Figure 9 shows the dependence of the grain desorption size at the far side of clumps of $R_{\text{cl}} = 0.1 \text{ pc}$ with the radiation strength (U_0) and gas density (n_{H}). The results

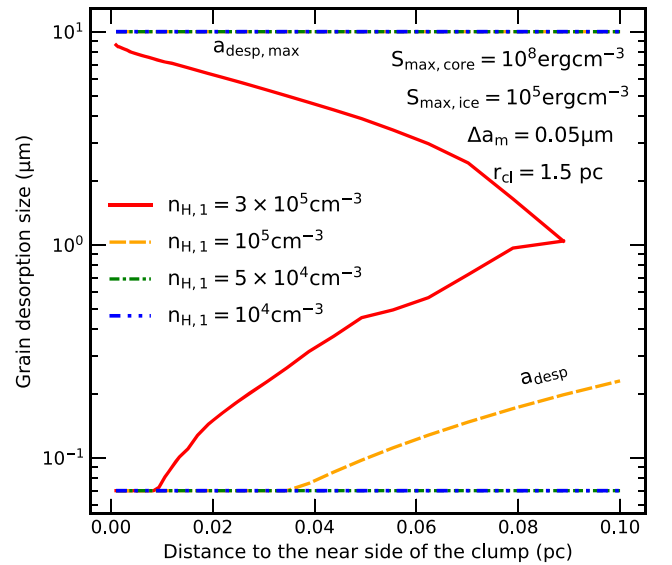
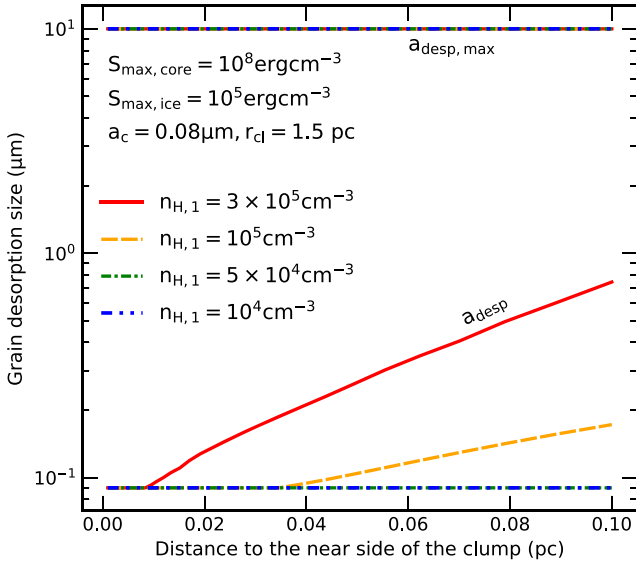
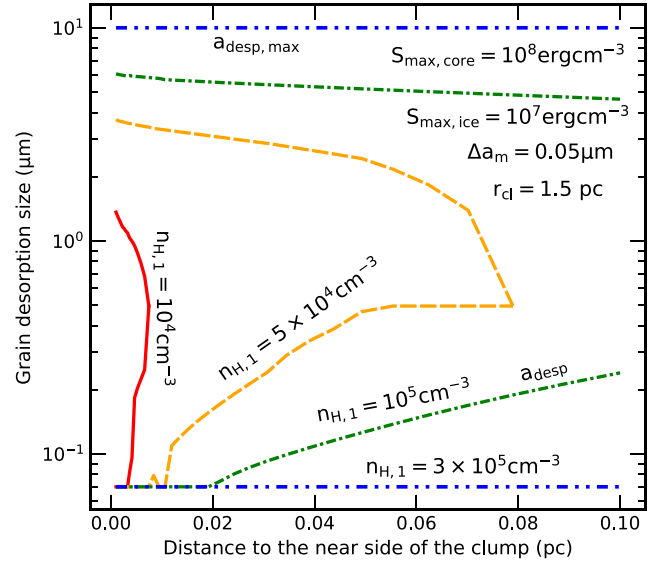
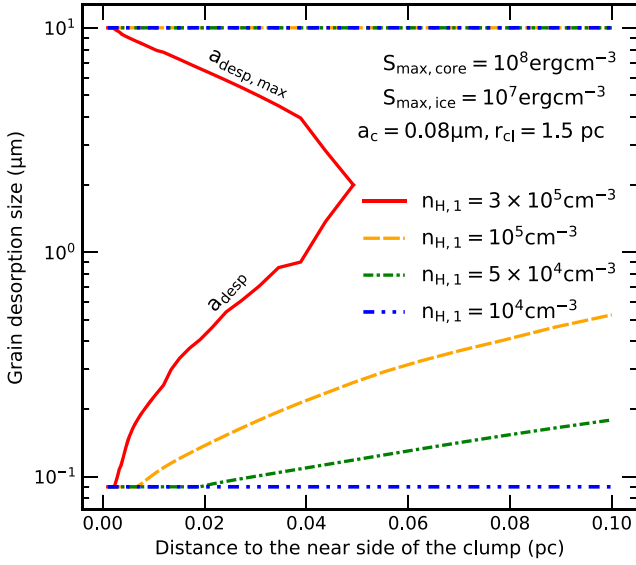


Figure 7. Variation of the range of desorption size of the icy grain mantles inside clumps at $r = 1.5$ pc for different gas density profiles, $S_{\max, \text{ice}} = 10^7 \text{ erg cm}^{-3}$ (upper panel) and $S_{\max, \text{ice}} = 10^5 \text{ erg cm}^{-3}$ (lower panel). The grain core is assumed to have $a_c = 0.08 \mu\text{m}$ and $S_{\max} = 10^8 \text{ erg cm}^{-3}$.

Figure 8. Similar results as Figure 7 but for icy grains with a fixed thickness of the ice mantle of $\Delta a_m = 0.05 \mu\text{m}$.

are for icy grains with a fixed $a_c = 0.08 \mu\text{m}$ and icy mantles with $S_{\max, \text{ice}} = 10^7 \text{ erg cm}^{-3}$ (left panel) and $S_{\max, \text{ice}} = 10^5 \text{ erg cm}^{-3}$ (right panel). Empty parts represent regions where water vapor cannot condense into ice, i.e., $T_{\text{dust}} > 170 \text{ K}$. Similar to the RATD effect, icy grain mantles inside clumps with low gas densities and with lower maximum tensile strengths $S_{\max, \text{ice}}$ are detached by rotational desorption stronger.

The lower panels in Figure 9 show similar results as the upper panels but account for the variation of clump size with distance given by the upper left panel of Figure 5. The sample of our studied cases (upper left panel of Figure 5) are also marked in the map. One can see that if $n_{\text{H},1} < 10^5 \text{ cm}^{-3}$, large icy grain mantles with $a \geq 0.5 \mu\text{m}$ will be strongly separated from the core even if they locate in large clumps at $r \sim 10 \text{ pc}$ ($U_0 \sim 10^3$). If the clumpy torus is denser with $n_{\text{H},1} \geq 3 \times 10^5 \text{ cm}^{-3}$, thick ice mantles up to micron sized can remain on the grain surfaces at the far side of clumps due to inefficient rotational desorption. Ice mantles with a

composite structure can be more easily detached from the cores by rotational desorption, but the difference is not clear (see the right panel). In this case, the presence of ice mantles increases the sticking coefficient that facilitates sticky collisions between icy grains to form larger dust aggregates. However, the increase in the size of the composite grains induces a decrease of the tensile strength. Consequently, newly formed large dust aggregates can be disrupted by RATD, which prevents grain growth and planet formation (see the lower left panel of Figure 5). However, the formation of large grains and further evolution can happen if the clumps are denser and bigger than in our consider cases.

4.3. Disruption and Desorption Timescales

Dust grains in the AGN torus may experience strong rotational damping due to IR reemission, i.e., $F_{\text{IR}} \geq 1$ (see Hoang et al. 2020 for an explanation). Thus, the moment when composite grains of size a are disrupted by RATD can be found by setting $\omega(t)$ given by Equation (4) to equal ω_{disr} given by

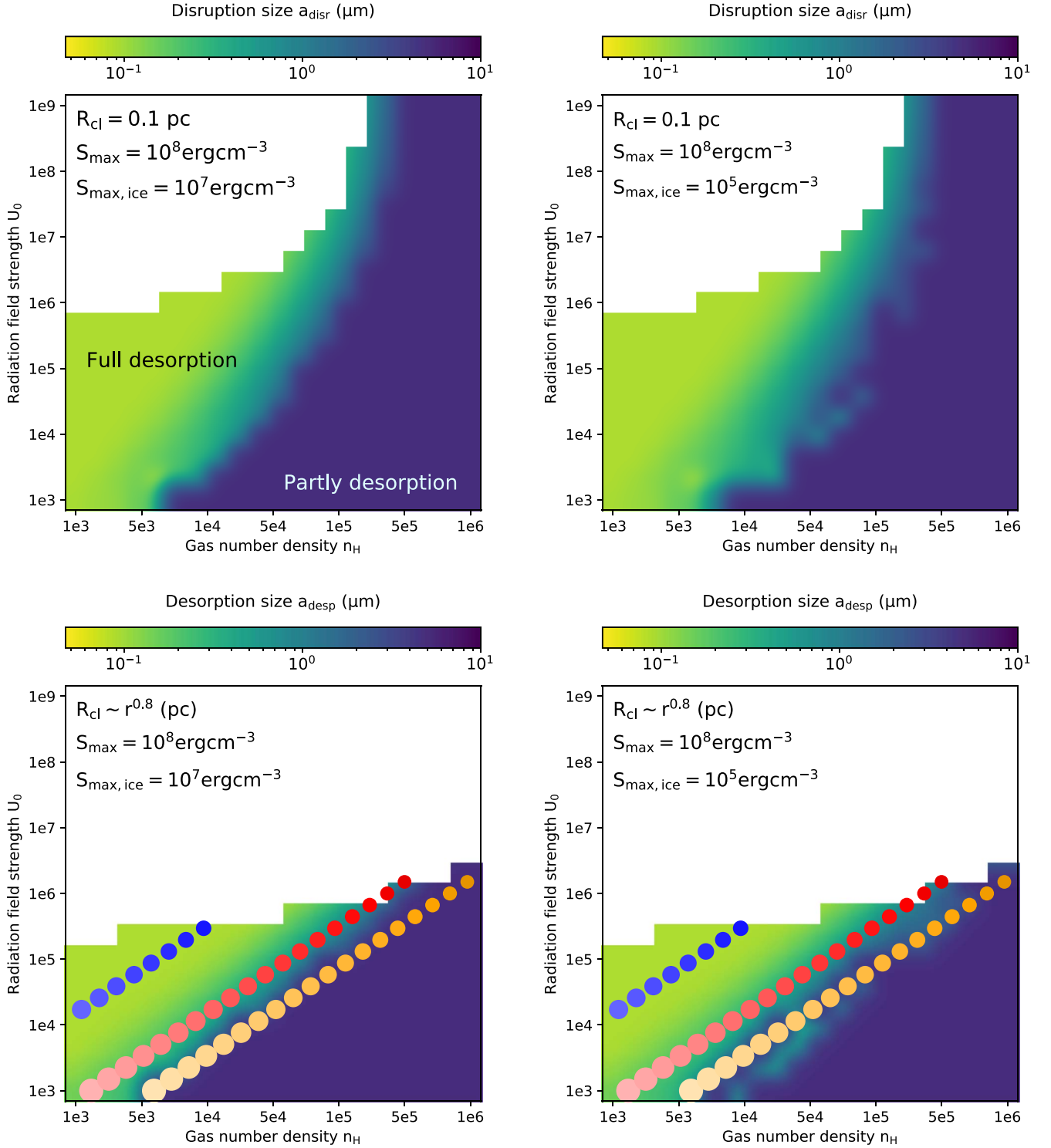


Figure 9. Upper panels: dependence of the grain desorption size of the icy grain mantles at the far side of clumps of size $R_{cl} = 0.1$ pc on the radiation strength U_0 and the gas density n_H , assuming $S_{max,ice} = 10^7 \text{ erg cm}^{-3}$ (left) and $S_{max,ice} = 10^5 \text{ erg cm}^{-3}$ (right) and assuming that the grain core is fixed at $a_c = 0.08 \mu\text{m}$ and has $S_{max} = 10^8 \text{ erg cm}^{-3}$. The snow line where ice can condense on the grain surfaces is the boundary between the white and colored regions. Green and blue colors imply the full desorption of ice mantles inside the clumps while dark blue implies desorption only on the front half of the clumps. Lower panels: similar to the upper panels but account for the variation of clump size with distance given by the upper left panel of Figure 5. The sample of our studied cases (upper left panel of Figure 5) is marked on the map.

Equation (10). The disruption time t_{disr} is given by:

$$t_{disr} = -\tau_{damp} \ln\left(1 - \frac{\omega_{disr}}{\omega_{RAT}}\right) \text{ s.} \quad (16)$$

Similarly, the moment when an ice mantle detaches from a solid grain core by rotational desorption can be found by setting $\omega(t) = \omega_{desp}$ (Equation (15)). The desorption time

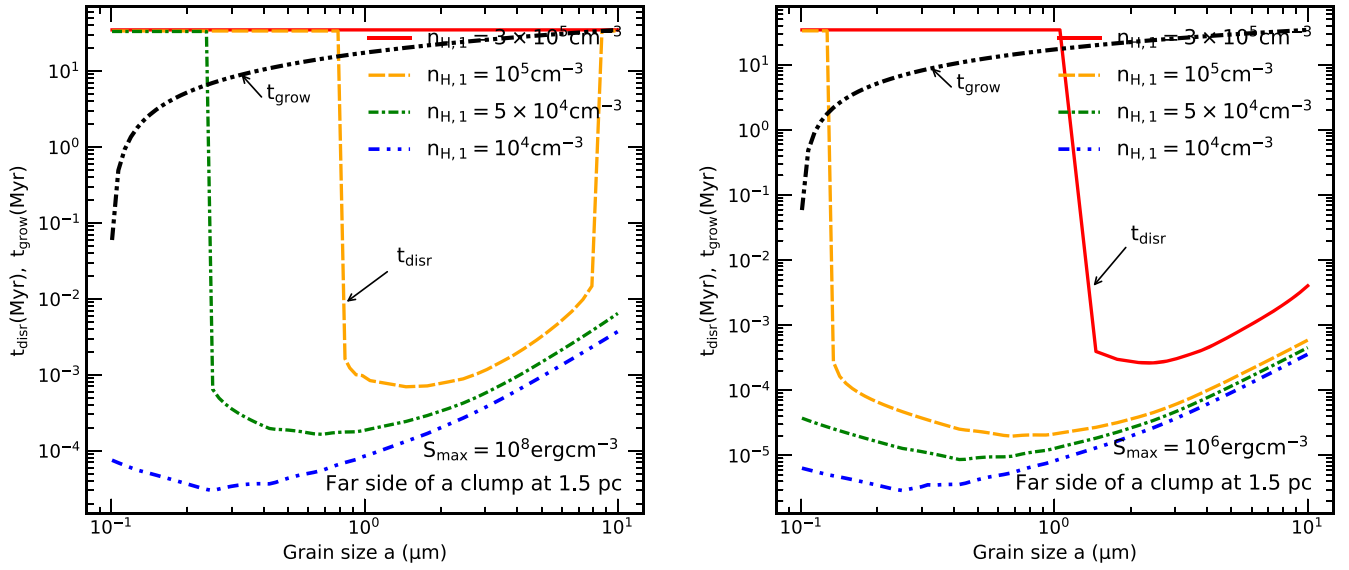


Figure 10. Dependence of the disruption timescale t_{disr} on grain size for composite dust grains at the far side of a clump of $R_{\text{cl}} = 0.05$ pc at $r = 1.5$ pc, assuming different gas densities $n_{\text{H},1}$, and $S_{\text{max}} = 10^8$ erg cm^{-3} (left panel) and $S_{\text{max}} = 10^6$ erg cm^{-3} (right panel). The growth timescale (black dashed–dotted–dotted line) of the corresponding grain size is plotted in the figure for comparison. Dust disruption only happens within \sim kiloyears, much shorter than the time required for grain growth.

t_{desp} is then:

$$t_{\text{desp}} = -\tau_{\text{damp}} \ln \left(1 - \frac{\omega_{\text{desp}}}{\omega_{\text{RAT}}} \right) \text{s}. \quad (17)$$

5. Grain Growth versus Disruption Time

In Sections 3.3 and 4.2, we study the effect of rotation disruption and desorption on composite and icy grains in the midplane of the torus and find that grain growth and planet formation can occur in the torus in the idealized smooth torus model. However, large composite grains and icy grain mantles of size $a \geq 1 \mu\text{m}$ are efficiently disrupted by RATs in the clumpy torus model, assuming the same gas density distribution adopted by Wada et al. (2019) and Wada et al. (2021). Thus, to check whether grain growth can occur in the clumpy torus, we will calculate the timescale of grain growth in the hit-and-stick stage and compare it with the timescale of dust destruction and ice desorption in Sections 5.1 and 5.2.

5.1. Grain Growth Timescale

Wada et al. (2019) considered the possibility that icy grain mantles (of initial size $a_0 \sim 0.1 \mu\text{m}$) in the torus can grow to larger ones via coagulation, assuming that grain growth follows the ballistic cluster-cluster aggregation (BCCA) model. The mass growth rate dm/dt during the hit-and-stick stage via the BCCA route is given by Wada et al. (2019, 2021):

$$\frac{dm}{dt} = \frac{2\sqrt{2\pi}\Sigma_{\text{d}}a^2\Delta v}{H_{\text{d}}}, \quad (18)$$

where Σ_{d} is the surface mass density, Δv is the relative velocity between dust aggregates, and H_{d} is the scale height of the dust disk.

The growth rate of grain size of a can be written as:

$$\frac{1}{a} \frac{da}{dt} = \frac{3}{8} \sqrt{\frac{\pi}{2}} \eta \sqrt{\alpha} R_{\text{c}}^{1/4} \sqrt{\frac{GM_{\text{BH}}}{R^3}}, \quad (19)$$

where η is the gas-to-dust mass ratio, α is a dimensionless parameter that determines the kinematic viscosity in the turbulent disk (Shakura & Sunyaev 1973), R_{c} is the Reynolds number, M_{BH} is the mass of the SMBH, and R is the distance from the AGN center.

The time required to form a dust aggregate of size a is given by (see the Appendix for a detailed derivation):

$$\begin{aligned} t_{\text{grow}}(a) &= \frac{8}{3\eta\alpha^{1/2}R_{\text{c}}^{1/4}} \sqrt{\frac{2}{\pi}} \ln \left(\frac{a}{a_0} \right) \left(\frac{GM_{\text{BH}}}{R^3} \right)^{-1/2} \\ &\approx 3.4489 \text{ Myr} \ln \left(\frac{a}{a_0} \right) \left(\frac{\eta}{0.01} \right)^{-1} \left(\frac{\alpha}{0.02} \right)^{-3/4} \\ &\times \left(\frac{M_{\text{BH}}}{10^6 M_{\odot}} \right)^{-3/8} \left(\frac{R}{\text{pc}} \right)^{9/8} \left(\frac{c_{\text{s}}}{1 \text{ km s}^{-1}} \right)^{-1/4}, \end{aligned} \quad (20)$$

where $a_0 = 0.1 \mu\text{m}$ is the radius of icy monomers and c_{s} is the sound velocity.

5.2. Comparison of Grain Growth to the Rotational Disruption and Desorption Timescales

5.2.1. Growth and Disruption Timescales

The left panel of Figure 10 shows the growth (gray lines) and disruption timescales (color lines) of different grain sizes varying from $a = 0.1 \mu\text{m}$ to $a = 10 \mu\text{m}$ at the far side of a clump of radius $R_{\text{cl}} = 0.05$ pc at $r = 1.5$ pc, assuming different gas density profiles and $S_{\text{max}} = 10^8$ erg cm^{-3} . For $n_{\text{H},1} = 3 \times 10^5 \text{ cm}^{-3}$, dust aggregates in the far side of the clump can freely grow to micron-sized grains of $a \geq 10 \mu\text{m}$ due to inefficient RATD (see the left panel of Figure 3), i.e., $t_{\text{disr}} > t_{\text{grow}}$. By decreasing the gas density, submicron grains of $a < 1 \mu\text{m}$ can survive, but larger grains will be quickly disrupted by RATD just after $t_{\text{disr}} \sim$ kiloyear, much faster than grain growth of this size by a factor of $\sim 10^4$. The disruption time slightly increases for micron-sized grains, but it is still smaller than the growth time by a factor of ~ 3000 . By decreasing the gas density, dust grains of size $a > 0.1 \mu\text{m}$ become more difficult to form due to efficient RATD, i.e.,

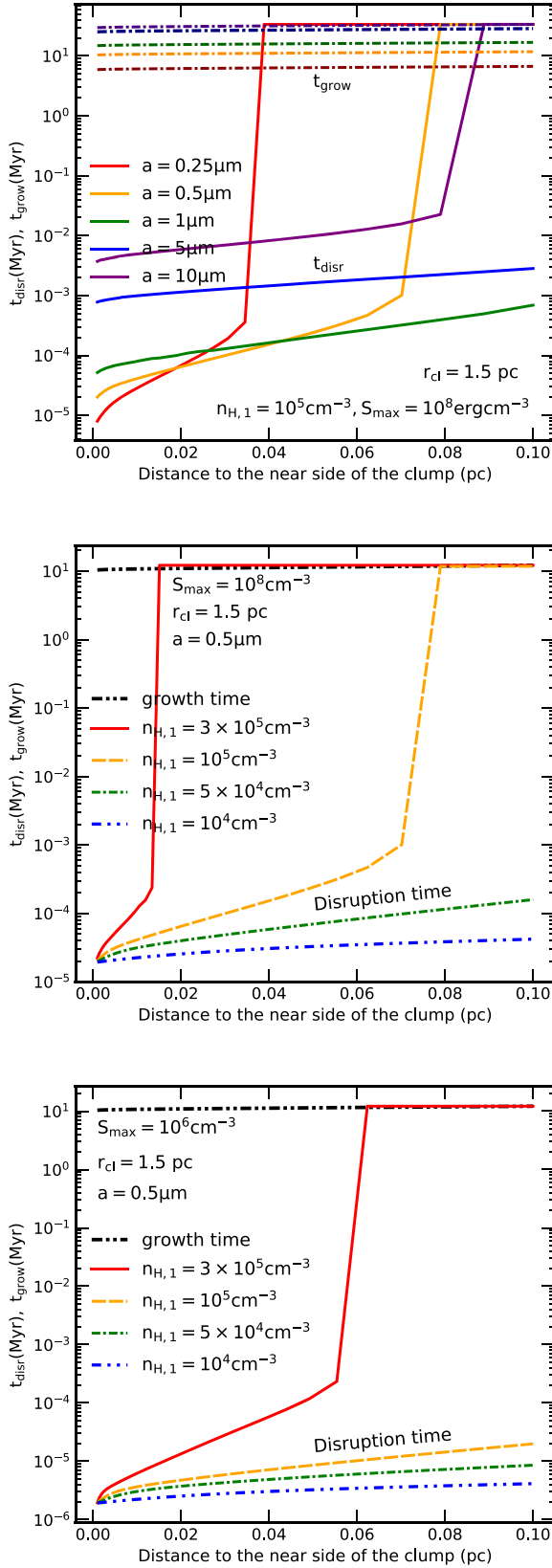


Figure 11. Comparison of the grain growth (black dashed–dotted lines) and disruption (colored lines) timescales of composite grains as a function of distance within a clump of radius $R_{\text{cl}} = 0.05 \text{ pc}$ located at $r = 1.5 \text{ pc}$ from the AGN center. The upper panel shows the timescale for different grain sizes. The central and lower panels are for grains of size $a = 0.5 \mu\text{m}$ with different gas density profiles, $S_{\text{max}} = 10^8 \text{ erg cm}^{-3}$ and 10^6 erg cm^{-3} , respectively.

smaller t_{disr} . The big gap between the growth and disruption timescale for grains within a disrupted range of $a_{\text{disr}} \leq a \leq a_{\text{disr,max}}$ implies the significant suppression of grain growth via coagulation for the clumpy torus model.

The right panel of Figure 10 shows similar results as the left panel but for dust grains with a lower strength of $S_{\text{max}} = 10^6 \text{ erg cm}^{-3}$. For the same density $n_{\text{H},1} = 3 \times 10^5 \text{ cm}^{-3}$, composite dust grains can freely grow to $a \sim 1 \mu\text{m}$, but further growth will be prevented by the RATD effect, i.e., $t_{\text{disr}} < t_{\text{grow}}$ by a factor of ≥ 3000 . Dust disruption inside the clumps happens stronger (i.e., smaller a_{disr}) and quicker (i.e., smaller t_{disr}) for more dilute clumps. This feature implies the difficulty for large dust aggregates to survive in the clumpy torus model.

The upper panel of Figure 11 shows the space-varying growth (faint lines) and disruption (dark lines) timescales for different grain sizes inside a clump at $r = 1.5 \text{ pc}$, assuming $S_{\text{max}} = 10^8 \text{ erg cm}^{-3}$. One can see that the disruption timescale is different for different grain sizes and different locations inside the clumps. But generally, composite dust grains within the disrupted range $a_{\text{disr}} - a_{\text{disr,max}}$ (the left panel of Figure 3) will be destroyed by RATD before they can grow to larger sizes (i.e., $t_{\text{disr}} < t_{\text{grow}}$, a factor of $\geq 10^3$). Otherwise, they are not affected by RATD and can collide with another to form larger ones (i.e., the presence of grain of sizes $a < 0.5 \mu\text{m}$ and $a \sim 10 \mu\text{m}$) at the far side of clumps (the yellow curve in the left panel of Figure 12).

The center panel of Figure 11 compares t_{grow} with t_{disr} for composite grains of size $a = 0.5 \mu\text{m}$ with $S_{\text{max}} = 10^8 \text{ erg cm}^{-3}$ inside clumps at $r = 1.5 \text{ pc}$, assuming different gas density profiles, $n_{\text{H},1}$. By reducing the gas density, grains of size $a = 0.05 \mu\text{m}$ will be destroyed by RATD quicker (i.e., smaller $t_{\text{disr}} < 1000 \text{ yr}$) and stronger (i.e., RATD happens at the far face of the clump). Similarly, the timescale for dust disruption by RATD is shorter for dust grains with a lower tensile strength (e.g., porous structures) (see the lower panel with $S_{\text{max}} = 10^6 \text{ erg cm}^{-3}$).

5.2.2. Growth and Desorption Timescales

Figure 12 shows the grain growth (gray line) and desorption (color lines) timescales for different sizes of icy grain mantles located at the far side of clumps at $r = 1.5 \text{ pc}$, assuming $S_{\text{max,ice}} = 10^7 \text{ erg cm}^{-3}$ and 10^5 erg cm^{-3} for the left and right panel, respectively. The dark and faint lines present the case of a fixed grain core and fixed ice mantle thickness. For a dense clump with $n_{\text{H},1} = 3 \times 10^5 \text{ cm}^{-3}$, ice can form and freely cover all grain sizes without separating due to inefficient rotation desorption. For clumps with $n_{\text{H},1} = 10^5 \text{ cm}^{-3}$, ice can cover solid grain cores up to sizes of $a < 0.8 \mu\text{m}$, but thicker ice mantles (larger size of icy grains) will be quickly detached (i.e., $t_{\text{desp}} < t_{\text{grow}}$), just after few kiloyears. By decreasing the gas density and $S_{\text{max,ice}}$, more grain core–ice mantle structures will be destroyed (i.e., extended $a_{\text{desp}} - a_{\text{desp,max}}$) over shorter timescales (i.e., smaller t_{desp}). However, thin ice mantles are desorbed by rotational desorption more weakly, i.e., a longer desorption timescale (dashed lines) and thus, may be unaffected in dense clumps, i.e., $n_{\text{H}} \geq 3 \times 10^5 \text{ cm}^{-3}$, even if $S_{\text{max,ice}}$ is reduced from $S_{\text{max,ice}} = 1 \times 10^7 \text{ erg cm}^{-3}$ to $S_{\text{max,ice}} = 1 \times 10^5 \text{ erg cm}^{-3}$.

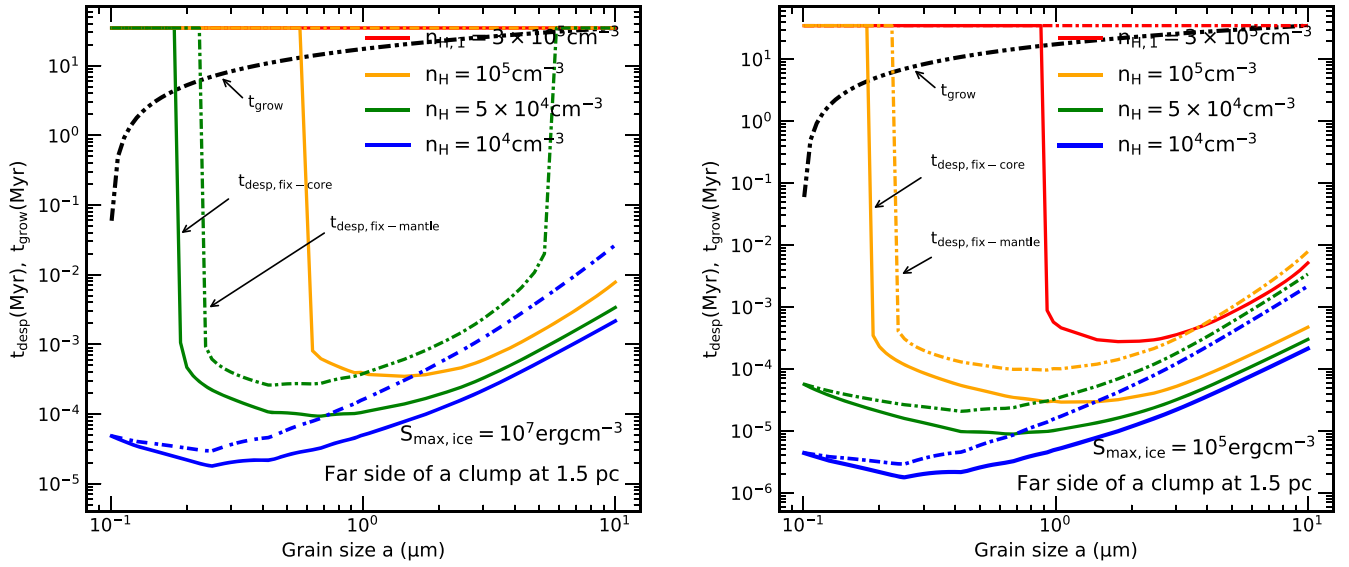


Figure 12. Variation of the grain growth (black dashed–dot–dot line) and rotational desorption timescales of different grain sizes at the far side of clumps of $R_{cl} = 0.05$ pc at $r = 1.5$ pc, assuming different gas density profiles, $S_{max,ice} = 10^7$ erg cm^{-3} (left panel) and 10^5 erg cm^{-3} (right panel). The solid lines show the results for icy grains with a fixed grain core of $a_c = 0.08$ μm while the dashed–dot lines are for the case of a fixed ice mantle thickness of $\Delta a_m = 0.05$ μm . Similar to RATD, the separation of the ice mantle from the grain core happens quickly just after a few kiloyears.

The upper panel of Figure 13 shows the space-varying growth (dashed–dotted lines) and desorption (solid lines) timescales for different sizes of icy grain mantles inside a clump of size $R_{cl} = 0.05$ pc at $r = 1.5$ pc, assuming a fixed grain core and $S_{max,ice} = 10^7$ erg cm^{-3} . Similar to the disruption timescale properties, icy grain mantles inside the desorption range $a_{desp} - a_{desp,max}$ (the left panel of Figure 3) will be detached by rotational desorption before they can grow to larger sizes. Otherwise, ice still can cover the grain cores and support the grain growth process. For example, ice can cover a grain core of $a \geq 2$ μm with a thickness of $\Delta a_m = 0.05$ μm at the back side of a clump due to inefficient rotational desorption on removing thin ice mantles.

Figure 14 shows the space-dependence of the growth (black dashed–dotted–dotted line) and desorption (color lines) timescales of icy grain mantles of size $a = 0.5$ μm inside a clump at $r = 1.5$ pc. We consider different gas density profiles and maximum tensile strengths of the ice mantles of $S_{max,ice} = 10^7$ erg cm^{-3} (upper panel) and $S_{max,ice} = 10^5$ erg cm^{-3} (lower panel). The solid and dashed lines present the case of a fixed grain core and fixed thickness of the ice mantles, respectively. One can see that rotational desorption destroys the grain core–ice mantle structure stronger and quicker at the near face of clumps due to a higher radiation flux. In addition, this effect will occur stronger, i.e., lower t_{desp} and a larger portion of influenced clumps, with decreasing gas density, decreasing maximum tensile strength, and increasing thickness of the ice mantles.

In conclusion, in the active region of rotational disruption and desorption, large composite/icy dust grains only take about a few thousand years to be rotationally disrupted/desorbed. The timescale is longer for optically thick regions and for grains with compact structures, but is generally shorter than the growth time of the same size by a factor of $\geq 10^3$. This implies that rotational disruption and desorption is a strong constraint for dust properties and evolution around intense radiation fields, which cannot be neglected when studying grain growth around low-luminosity AGN.

6. Discussion

6.1. Dust and Ice Evolution under AGN Radiation Feedback

Dust in the torus is a key component in the unified model of AGN (Antonucci 1993; Urry & Padovani 1995) and responsible for the “infrared bump” feature in the observed SEDs (Barvainis 1987; Urry & Padovani 1995; Fritz et al. 2006; Nenkova et al. 2008b; Stalevski et al. 2012). In addition, dust polarization induced by aligned dust grains is an important tool to study magnetic fields in AGN tori. Understanding the dust’s properties and its interactions with the AGN’s radiation field is key for constraining the feeding and feedback of the AGN to the surrounding environment and probing the origin of the central engine. However, detailed knowledge about the dust’s properties that are subject to AGN radiation feedback is still poorly constrained.

Previously, dust destruction due to AGN radiative feedback was studied by Barvainis (1987) via thermal sublimation and by Tazaki et al. (2020) for Coulomb explosions. However, these mechanisms only work in a small region near the AGN and effectively for small grains of $a \leq 0.1$ μm , and the Coulomb explosion effect is ineffective in an optically thick torus (Tazaki et al. 2020). Thus, dust grains beyond the sublimation front are hardly affected by AGN radiation feedback because of the high attenuation of X-ray and UV photons.

Nevertheless, Hoang et al. (2019b) realized that dust grains subjected to a strong radiation field can be rotationally disrupted by the RATD effect. Applying this mechanism to the smooth torus model of AGN with a high luminosity of $L_{bol} = 10^{46}$ erg s^{-1} , Giang & Hoang (2021) found the significant removal of large grains of $a \geq 1$ μm up to a boundary region of ~ 10 pc, for a wide range of maximum tensile strengths of $S_{max} = 10^7 - 10^{10}$ erg cm^{-3} and gas density distributions of $n_{H,1} = 6 \times 10^4 - 4 \times 10^5$ cm^{-3} . The reduction of the maximum grain size to $a_{max} < 10$ μm by RATD is more effective in higher latitude regions due to the lower gas density. However, for AGN with a low luminosity of

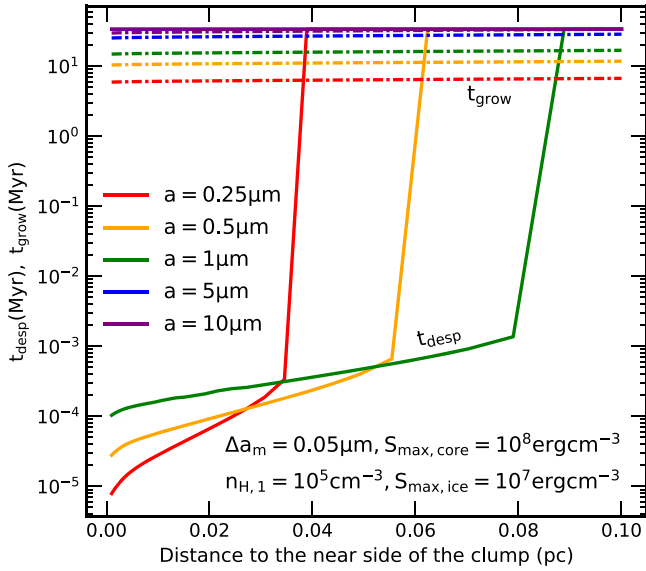
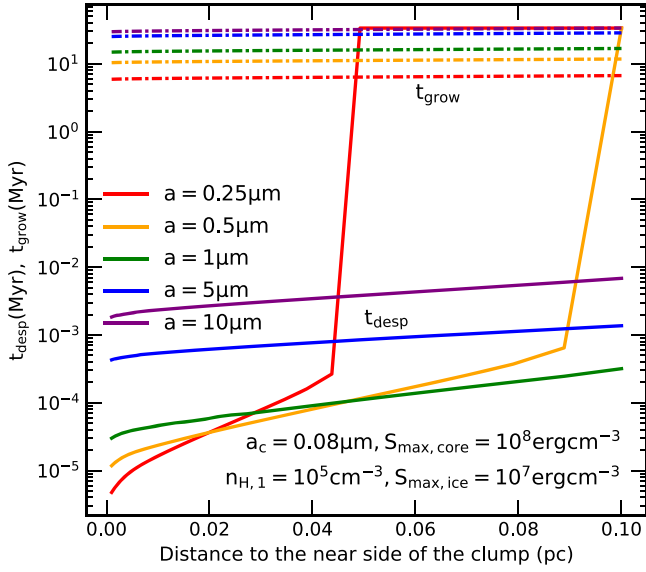


Figure 13. Upper panel: comparison between the variation of rotational desorption (solid lines) and grain growth timescales (dashed-dotted lines) of different grain sizes inside a clump at $r = 1.5$ pc, assuming $n_{H,1} = 10^5 \text{ cm}^{-3}$, icy grains with a fixed grain core of $a_c = 0.08 \text{ } \mu\text{m}$, and ice mantles with $S_{\text{max,ice}} = 10^7 \text{ erg cm}^{-3}$. Lower panel: similar results as the upper panel but for the case of a constant ice mantle thickness of $\Delta a_m = 0.05 \text{ } \mu\text{m}$.

$L_{\text{bol}} = 10^{42} \text{ erg s}^{-1}$, RATD is not efficient for the smooth torus model with a high gas density of $n_{H,1} > 5 \times 10^3 \text{ cm}^{-3}$ (Section 3.3.1). As a result, dust properties at the parsec scale in the midplane are not affected by RATD.

In contrast, if dust and gas are concentrated into dense clumps (i.e., the clumpy torus model), the attenuation of AGN radiation is reduced, and dust grains can still be spun up to the disruption limit by RATs. Consequently, RATD is strong enough to destroy composite dust grains in both dense clumps near the AGN center and large, dilute clumps at large distances of $r \sim 10$ pc (Section 3.3.2). The significant influence of RATD on the parsec scale of the torus arises from the fact that RATD can work with optical–NIR photons that can propagate to longer distances compared to X-rays and UV photons required for sublimation and Coulomb explosions. Moreover, RATD

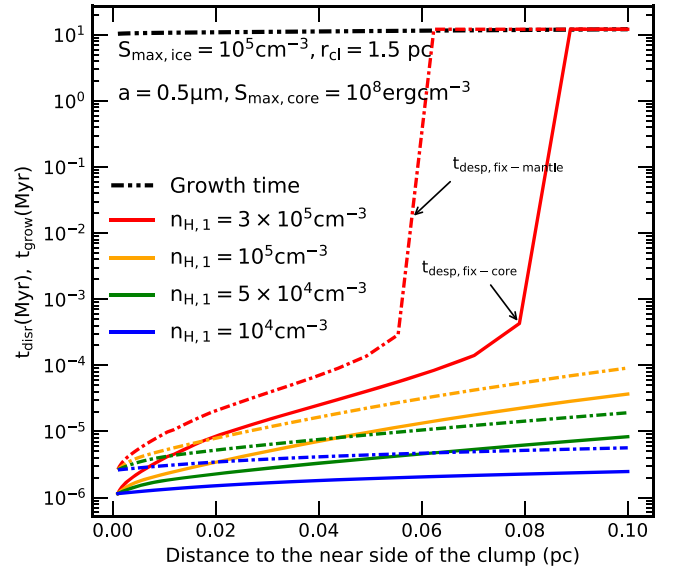
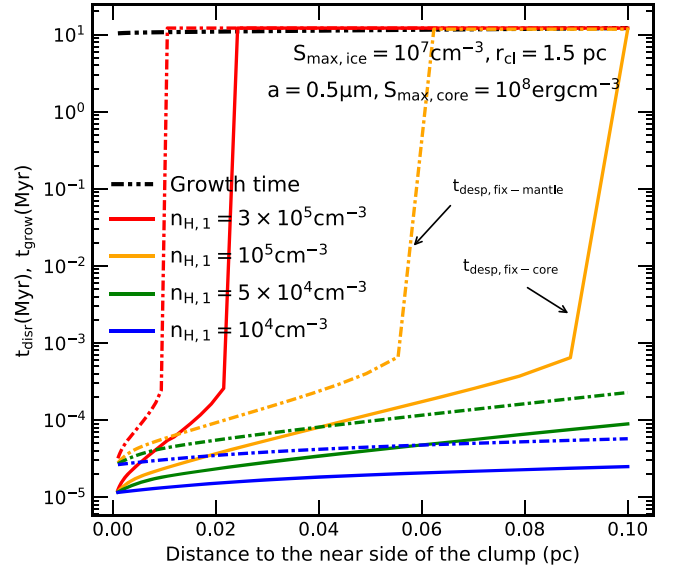


Figure 14. Variation of rotational desorption timescales for icy grain mantle of size $a = 0.5 \text{ } \mu\text{m}$ inside a clump at $r = 1.5$ pc with different gas density profiles, for ice mantles with $S_{\text{max,ice}} = 10^7 \text{ erg cm}^{-3}$ (upper panel) and $S_{\text{max,ice}} = 10^5 \text{ erg cm}^{-3}$ (lower panel), respectively. A comparison between the removal of ice mantles on a fixed grain core of $a_c = 0.08 \text{ } \mu\text{m}$ (solid lines) and a fixed ice mantle thickness of $\Delta a_m = 0.05 \text{ } \mu\text{m}$ (dashed-dot lines) is also presented.

depends sensitively on the grain structure and can disrupt large grains of composite structures in just a few thousand years. The dust properties modified by RATD would have important effects on the observational properties (emission and polarization; e.g., Lee et al. 2020), dust dynamics, and radiation pressure feedback (e.g., Hoang 2021). A detailed study of these effects will be presented in a follow-up paper.

On the other hand, icy grain mantles are expected to exist in the torus beyond the sublimation front (i.e., “original” snow line). However, rapidly rotating icy grain mantles induced by RATs may be rotationally desorbed by centrifugal forces (Hoang & Tram 2020; Tung & Hoang 2020). For low-luminosity AGN, we find that rotational desorption on icy grain mantles is inefficient for the smooth torus model

(Section 4.2.1). However, for the clumpy torus model, ice mantles can be desorbed from the grain cores beyond the “original” snow line, and the amount of icy grain mantles will decrease inside the clumps (Section 4.2.2). Similar to RATD, rotational desorption works with optical–NIR photons and only takes a few thousand years to detach icy grain mantles, shorter than the growth time by a factor of $\geq 10^3$ (see Section 5.2.2). These effects have important implications for accurately constrains on the abundance of water and complex molecules and the efficiency of grain coagulation in the torus.

It is worth noting that, in Section 4.2, we studied the effect of rotational desorption and found that this mechanism only can remove thick ice mantles of $\Delta a_m > 0.1 \mu\text{m}$. Icy dust aggregates with thin ice mantles still survive beyond the “original” snow line. However, thin ice mantles can be detached from the grain cores when accounting a reduced binding energy between icy particles due to the spinning effect, which is termed as the rotational desorption mechanism (Hoang & Tung 2019).

6.2. Dynamical Barriers of Planet Formation around an SMBH

Wada et al. (2019, 2021) studied the formation of blanets beyond the snow lines of the midplanes of torus regions around SMBHs from the hit-and-stick stage to the gravitational instability phase. The authors found that blanets can form if the AGN luminosity is at a low of $L_{\text{bol}} \sim 10^{42} \text{ erg s}^{-1}$, and the gas density is at a high of $n_{\text{H},1} \sim 10^5 \text{ cm}^{-3}$. The authors also studied whether grain shattering due to high-velocity collisions could be a critical barrier for blanet formation in the AGN torus. They found that grain fragmentation is inefficient due to the low relative velocity between icy dust aggregates. Particularly, the grain relative velocity, Δv , is found to span from $\sim 0.1\text{--}0.3 \text{ m s}^{-1}$ during the hit-and-stick stage to a maximum velocity of $\sim 57 \text{ m s}^{-1}$ at the end of gas compression stage, which is much lower than the critical velocity of shattering of $v_{\text{crit}} \sim 80 \text{ m s}^{-1}$. The value of Δv increases with increasing turbulence, whereby a higher viscosity of gas of $\alpha > 0.04$ results in the fragmentation of dust aggregates at kilometer sizes (Wada et al. 2021). However, during the hit-and-stick stage considered in this paper, the value of Δv is much smaller than the shattering threshold, implying that grain shattering is not an important barrier for blanet formation.

In this paper, we study the influence of rotation disruption on composite grains in the circumnuclear region with the same conditions adopted by Wada et al. (2019, 2021). We found that, for the smooth torus model with the high density of $n_{\text{H},1} \sim 10^5 \text{ cm}^{-3}$ adopted from Wada et al. (2019), a high attenuation of AGN radiation will reduce the efficiency of RATD (Section 3.3.1) at the parsec scale. Thus, RATD is not the major barrier for grain growth and blanet formation around low-luminosity AGN. However, the RATD mechanism is still a critical barrier of blanet formation around standard AGN, i.e., $L_{\text{bol}} > 1 \times 10^{42} \text{ erg s}^{-1}$.

In contrast, for the clumpy torus model, the presence of dust aggregates of $a \geq 1 \mu\text{m}$ inside clumps is almost prohibited by RATD, up to $r \sim 10 \text{ pc}$ (Section 3.3.2). Inside big clumps of $R_{\text{cl}} \sim 0.1 \text{ pc}$ with a high density of $n_{\text{H}} \sim 10^4 \text{ cm}^{-3}$, grain growth can occur at the far side of clumps due to inefficient RATD (the left panel of Figure 3, and the upper left panel of Figure 4). However, the growth of dust aggregates is accompanied by a decrease of internal density due to an increase of voids between monomers (Dominik & Tielens 1997;

Wada et al. 2008; Suyama et al. 2012; Shen et al. 2008). An increase of porosity P of large dust aggregates thus implies a significant reduction of the maximum tensile strength of $S_{\text{max}} \sim 10^6(1 - P)a_0^{-2}$ with a_0 the size of the monomer (Greenberg et al. 1995; Li & Greenberg 1997; Hoang 2019), and the enhancement of dust disruption by RATD (see the right panel of Figure 3 and the upper right panel of Figure 4). Newly formed dust aggregates are destroyed and the maximum size decreases to the pre-growth size. Moreover, the clear difference between the disruption timescale (a few thousand years) and the growth timescale (a few million years) (Section 5.2.1) sets the first barrier that dust must overcome to continue blanet formation.

On the other hand, grain growth is expected to occur more efficiently beyond the snow line where the presence of ice mantles increases the sticking coefficient and prevents fragmentation during collisions between submicron composite dust grains, which facilitates the formation of large, highly porous dust aggregates (Chokshi et al. 1993; Gundlach et al. 2011). In Section 4.2.1, we show that rotational desorption is not a major barrier for grain growth at the parsec scales if gas and dust distribute smoothly in space. However, if they concentrate into dense clumps within the diffuse torus, ice mantles will quickly be separated from the grain core (Section 4.2.2). The removal of ice mantles thus may cause the dust grains to bounce off each other rather than sticking together or grain shattering (see Chiang et al. 2010), which would reduce the efficiency of grain growth to large aggregates of micrometer to centimeter sizes. Furthermore, ice mantles are detached from the solid grain core after just a few thousand years (Section 5.2.2), which sets a second barrier for blanet formation around low-luminosity AGN.

6.3. Effects of Torus Models on Rotational Disruption and Desorption

Indeed, the real morphology and distribution of dust and gas inside the circumnuclear region is still debated. The smooth torus model generally can reproduce the observed IR SEDs of a large sample of AGN and the absorption feature of SiO at $10 \mu\text{m}$ toward type II Seyfert galaxies (Fritz et al. 2006; Schartmann et al. 2008). However, Schartmann et al. (2008) showed that the width of the SED produced by the smooth torus model is narrower than observations (Granato & Danese 1994; Granato et al. 1997), and this model cannot explain the weak emission/absence of the SiO emission at $10 \mu\text{m}$ in Type I Seyfert galaxies (Hao et al. 2007; Siebenmorgen et al. 2005). The clumpy torus model proposed by Nenkova et al. (2002) can successfully explain these puzzles, and it also can explain the detection of multi-temperature components at the same distance in the circumnuclear region (Nenkova et al. 2008a, 2008b, Dullemond & van Bemmell 2005; Hönig et al. 2006; Stalevski et al. 2012). However, interferometric observations toward torus regions do not clearly show the discrete distribution of clumps inside the diffuse medium as illustrated in the clumpy torus model. They reveal a complex, inhomogeneous dust density distribution (Tristram et al. 2009; Shi et al. 2006; Hicks et al. 2009, (Markowitz et al. 2014; Izumi et al. 2018), that matches with the multi-gas-phase picture driven by the “radiation-driven fountain” model proposed by Wada et al. (2009) (Wada et al. 2016; Schartmann et al. 2014). This model also can reproduce the dependence of the observed properties of Type 1 and 2

Seyfert galaxies on luminosity (Burlon et al. 2011; Buchner et al. 2015) and the X-ray continua observed toward AGN (Buchner et al. 2021).

The simple smooth and clumpy torus distribution adopted in this paper may overestimate the active region of rotational disruption and desorption on composite and icy dust grains in the circumnuclear region. In addition, we also only solve the radiative transfer of AGN radiation in one dimension, which basically neglects the asymmetric geometry of AGN radiation emitting from the accretion disk, and the detailed dust scattering and thermal dust emission in three dimensions. Thus, a detailed study with a more realistic model of the AGN radiation field and dust/gas distribution in the torus region is required to constrain better the effect of RATD and rotational desorption in the torus region. This is the key for answering the question of blanet formation in low-luminosity AGN.

6.4. Upper Limit of RATD for the Clumpy Torus Model

From Figure 4, one can see a decrease of the RATD efficiency inside clumps with decreasing radiation strength and increasing gas density. With the gas profile adopted from Wada et al. (2016, 2019) and the clump size distribution adopted in the lower panel of Figure 4, one can see that rotational disruption and desorption are the main barriers for grain growth and blanet formation.

However, if the clumps are bigger (i.e., higher β_{cl} in Equation (5)) and have a higher gas density of $n_{\text{H}} > 3 \times 10^5 \text{ cm}^{-3}$, the RATD efficiency will be similar as in the smooth torus model. Large grains in the near face of clumps can be destroyed by RATD due to a higher radiation flux, but they can freely grow and form highly porous dust aggregates, i.e., micrometer to centimeter sizes, if they are located at the far side of clumps. For example, at $r = 1.5 \text{ pc}$ (corresponding to $U_0 = 2 \times 10^5$), with $n_{\text{H},1} = 3 \times 10^5 \text{ cm}^{-3}$, grain growth via coagulation will be prevented by RATD inside clumps of size $R_{\text{cl}} = 0.1 \text{ pc}$ (the upper panels of Figure 4), but it can occur normally and form blanets if the clumps are larger with $R_{\text{cl}} \geq 0.2 \text{ pc}$ or $n_{\text{H},1} > 10^6 \text{ cm}^{-3}$. On the other hand, a lower radiation field strength (i.e., lower AGN luminosity) also reduces the RATD effect and supports blanet formation inside the circumnuclear region.

The presence of more than one clump along the same radial direction is another factor that reduces the RATD efficiency, especially if the line of sight passes through many small but very dense clumps near the center region. Accounting for this effect will narrow the configurations supporting the global effect of RATD inside the torus but broaden the conditions that support grain growth and blanet formation.

6.5. RATD by IR Emission from Hot Dust Grains

In contrast to other dust-destruction mechanisms (i.e., thermal sublimation and Coulomb explosion) that require X-ray and extreme-UV radiation (Barvainis 1987; Tazaki et al. 2020), RATD can work with low-energy photons at optical–IR wavelengths (Hoang et al. 2020), resulting in the significant effect of RATD at the parsec scale inside torus regions. However, in Sections 3.3 and 4.2, we only consider the disruption effect by optical–mid-IR radiation produced by the accretion disk and neglect IR emission from the hot dust near the sublimation front.

Near-IR–submillimeter radiation can penetrate deeply in dense environments so that the additional contribution from thermal dust emission basically extends the active region of rotational disruption and desorption in the circumnuclear region. In particular, large micron-sized grains are mainly spun up by near-IR–submillimeter radiation, that the enhanced IR radiation by thermal dust grains will strengthen the RATD effect on destroying large micron-sized composite grains and the rotational desorption effect on removing large icy grain mantles. Consequently, rotational disruption and desorption can be the main barrier for blanet formation, even in the smooth torus region or in large clumps near the outer part of the torus. Detailed modeling accounting for the thermal emission of dust grains should be performed to quantify precisely when rotational disruption and desorption prohibit blanet formation around low-luminosity AGN.

6.6. Efficiency of RATD and Blanet Formation

The efficiency of RATD depends on the fraction of grains on high- J attractors, denoted by $f_{\text{high-}J}$, which in general depends on the grain properties (shape, size, and magnetic properties), with $0 < f_{\text{high-}J} \leq 1$ (Hoang 2020; Lazarian & Hoang 2021). The extensive study for numerous grain shapes and compositions by Herranen et al. (2021) found $f_{\text{high-}J} \sim 0.2 - 0.7$, depending on the grain shapes, sizes, and radiation field. The presence of iron inclusions was found to increase $f_{\text{high-}J}$ to unity (Hoang & Lazarian 2016), whereas carbonaceous grains have a lower fraction of $f_{\text{high-}J} < 1$. Therefore, the RATD mechanism prohibits the formation of blanets out of composite grains with iron inclusions, but it does not completely rule out the formation of blanets made of purely carbonaceous material. However, dust grains in the dense torus are presumably present in a composite dust instead of two separate silicate and carbonaceous grain materials. Therefore, the efficiency of blanet formation via dust coagulation around SMBHs is reduced by the RATD effect, especially in standard AGN with $L_{\text{bol}} > 10^{42} L_{\odot}$.

7. Summary

Previous studies suggest that planets can form in the torus of low-luminosity AGN around SMBHs. Here we have studied the effect of rotational disruption and desorption of dust and ice by RATs due to AGN radiation feedback and discussed their implications for grain growth and planet formation around SMBHs. Our main findings are summarized as follows:

1. For the simplified smooth model of a torus with a gas density profile of $n_{\text{H}} = n_{\text{H},1}(r/1 \text{ pc})^{-3/2}$ and a gas density at 1 pc of $n_{\text{H},1} = 10^4 - 10^5 \text{ cm}^{-3}$, as adopted from Wada et al. (2019), rotational disruption and desorption are only efficient at distances of $r < 1 \text{ pc}$ for low-luminosity AGN of $L_{\text{bol}} \sim 10^{42} \text{ erg s}^{-1}$. These rotational effects are not efficient for disrupting large grains at large distances of $r > 1 \text{ pc}$ due to the high extinction of stellar radiation by intervening dust. Therefore, grain growth and blanet formation can occur around low-luminosity AGN as suggested by Wada et al. (2019).
2. For the model where gas and dust concentrate into dense clumps that are distributed diffusely inside the circumnuclear region, the attenuation of the AGN radiation is reduced, which enhances the spinning rate of the dust grains. As a result, the efficiency of rotational disruption

of composite grains and the desorption of ice mantles increase. The sticking coefficient between monomers during the collisions would be reduced due to the removal of ice mantles around the grain cores, and the increase in size of dust aggregates is suppressed by RATD to $a_{\max} < 10 \mu\text{m}$ even in large clumps of $R_{\text{cl}} \sim 0.2 \text{ pc}$ at $r = 10 \text{ pc}$, assuming the same gas density distribution adopted from Wada et al. (2019). The timescales of rotational disruption and desorption are shorter than the growth timescale by a factor of $\geq 10^3$, such that rotational disruption and desorption become a major barrier for grain growth and blanet formation in the AGN torus.

3. Grain growth and blanet formation may occur inside large clumps of $R_{\text{cl}} > 0.1 \text{ pc}$ with higher gas densities than the ones adopted for our modeling. In addition, since the observations support an inhomogeneous, multi-gas-phase structure of torus regions driven by the ‘‘radiation-driven fountain’’ model, detailed calculations with more a realistic AGN source and torus model, and the additional contribution of IR dust radiation are required to determine whether grain growth and blanet formation can occur in the presence of grain rotational disruption/desorption.

We thank the referee for comments that helped improve the presentation of our paper. T.H. acknowledges the support of the National Research Foundation of Korea (NRF) grants funded by the Korean government (MSIT) through the Mid-career Research Program (2019R1A2C1087045).

Appendix

Hit-and-stick Timescale of the BCCA Model

In the blanet formation picture suggested by Wada et al. (2019), icy grain mantles in the midplane of the torus first collide and stick together via the BCCA model to form larger dust aggregates (Okuzumi et al. 2012). The maximum size at the end of this stage is about centimeter sized (Wada et al. 2019). Then, centimeter-sized grains continue to grow further via (2) gas pressure compression, (3) gravitational compression, and form Earth-sized blanets after (4) a gravitational instability phase (Goldreich & Ward 1973).

During the hit-and-stick stage, the radius of a BCCA cluster with N icy monomers and grain mass m is described as (Wada et al. 2008, 2009, 2019):

$$a = N^{0.5} a_0 = \left(\frac{m}{m_0} \right)^{0.5} a_0, \quad (\text{A1})$$

where $a_0 = 0.1 \mu\text{m}$ is the size of an icy monomer at which Wada et al. (2019) starts to track grain growth and $m_0 = 4/3\pi a_0^3 \rho_0$ is the mass of a monomer, with $\rho_0 = 1 \text{ g cm}^{-3}$ the mass density of ice.

The rapid increase in size of newly form dust aggregates is accompanied by a significant decrease of its mass density, which is:

$$\rho_{\text{int}} = \rho_0 \left(\frac{m}{m_0} \right)^{(1-3/D)}, \quad (\text{A2})$$

where $D \approx 1.9$ is the fractal dimension for dust aggregates formed via the BCCA model (Mukai et al. 1992; Okuzumi & Tanaka 2009).

From Equation (A1), the mass m of grain size a is given by:

$$m = m_0 \left(\frac{a}{a_0} \right)^2, \quad (\text{A3})$$

and its derivative is:

$$dm = \frac{m_0}{a_0^2} 2ada = \frac{4/3\pi a_0^3 \rho_0}{a_0^2} 2ada = \frac{4\pi \rho_0 a_0}{3} 2ada. \quad (\text{A4})$$

The growth rate of dust aggregates during the hit-and-stick stage is (Wada et al. 2021):

$$\frac{dm}{dt} = \frac{2\sqrt{2\pi} \Sigma_d a^2 \Delta v}{H_d}, \quad (\text{A5})$$

where $\Sigma_d = \Sigma_g \eta$ is the dust mass surface density, with $\Sigma_g = m_H N_H$ the gas mass surface density and N_H the gas column density, and $\eta = 0.01$, which is the typical dust-to-gas mass ratio in the interstellar medium. The second term $\Delta v \approx 1/2\sqrt{\alpha} c_s R_e^{1/4} S_t$ is the collision velocity between dust aggregates, with α the kinematic viscosity of the gas due to turbulence (Shakura & Sunyaev 1973). In our study, we adopt the similar value of $\alpha = 0.02$ as in the blanet paper of Wada et al. (2021). c_s is the sound velocity:

$$c_s = \sqrt{\frac{k_B T_{\text{gas}}}{\nu m_H}}, \quad (\text{A6})$$

where k_B is the Boltzmann constant, T_{gas} is the gas temperature in the torus given by Equation (2), and $\nu = 2$. R_e is the Reynolds number, which represents the ratio between the turbulent and the kinematic viscosities of gas in the torus:

$$R_e = \frac{\alpha c_s^2}{\nu \Omega_K} \approx 1.8 \times 10^3 \times \left(\frac{\alpha}{0.02} \right) \left(\frac{M_{\text{BH}}}{10^6 M_\odot} \right)^{-1/2} \left(\frac{R}{\text{pc}} \right)^{3/2} \left(\frac{c_s}{1 \text{ km s}^{-1}} \right), \quad (\text{A7})$$

where Ω_K is the orbital frequency of dust in the midplane of the torus, given as:

$$\Omega_K = \sqrt{\frac{GM_{\text{BH}}}{R^3}}, \quad (\text{A8})$$

where M_{BH} is the mass of the SMBH and R is the distance toward the AGN center. Assuming an Eddington ratio of 0.01, one gets $M_{\text{BH}} \sim 8 \times 10^5 M_\odot$ for AGN with $L_{\text{bol}} = 10^{42} \text{ erg s}^{-1}$.

The last term S_t in the equation of Δv is the normalized stopping time, i.e., the Stokes number, at which a dust particle couples with ambient gas, i.e., the velocity of the dust particle reaches maximum values due to gas drag, which is:

$$S_t = \frac{\pi \rho_{\text{int}} a}{2\Sigma_g}. \quad (\text{A9})$$

Lastly, the term H_d in Equation (A5) is the scale height of the dust disk, which is:

$$H_d = \left(1 + \frac{S_t}{\alpha} \frac{1 + 2S_t}{1 + S_t} \right)^{-1/2} H_g, \quad (\text{A10})$$

where H_g is the scale height of the gas disk, which is:

$$H_g = \frac{c_s}{\Omega_K}. \quad (\text{A11})$$

In the hit-and-stick stage, $S_t \ll 1$ and is nearly a constant with the growth of dust grains (see Wada et al. 2019, 2021). Thus, we can adopt $H_d \approx H_g$.

Then, substituting Equation (A4) to Equation (A5), the increase of grain size a with time t can be described as:

$$\frac{da}{dt} = \frac{3}{4} \sqrt{\frac{2}{\pi}} \frac{\Sigma_d \Delta v}{\rho_0 a_0 H_d} a, \quad (\text{A12})$$

or:

$$\frac{1}{a} \frac{da}{dt} = \frac{3}{8} \sqrt{\frac{\pi}{2}} \eta \sqrt{\alpha} R_e^{1/4} \sqrt{\frac{GM_{\text{BH}}}{R^3}}. \quad (\text{A13})$$

The growth timescale of size a thus is numerically calculated as:

$$\begin{aligned} t_{\text{grow}}(a) &= \frac{8}{3\eta\alpha^{1/2}R_e^{1/4}} \sqrt{\frac{2}{\pi}} \ln\left(\frac{a}{a_0}\right) \left(\frac{GM_{\text{BH}}}{R^3}\right)^{-1/2} \\ &\approx 3.4489 \text{ Myr} \ln\left(\frac{a}{a_0}\right) \left(\frac{\eta}{0.01}\right)^{-1} \left(\frac{\alpha}{0.02}\right)^{-3/4} \\ &\quad \times \left(\frac{M_{\text{BH}}}{10^6 M_\odot}\right)^{-3/8} \left(\frac{R}{\text{pc}}\right)^{9/8} \left(\frac{c_s}{1 \text{ km s}^{-1}}\right)^{-1/4}. \end{aligned} \quad (\text{A14})$$


We note that we derive the timescale of the size growth above from Equation (A5), not taking the timescale from Wada et al. (2021). From Equations (A5) and (A1), the mass growth rate is:

$$\begin{aligned} \frac{dm_d}{dt} &= \frac{2\sqrt{2\pi}\Sigma_d a_0^2 (m_d/m_0)\Delta v}{H_d} \\ &= \frac{2\sqrt{2\pi}\Sigma_d a_0^2 m_d \Delta v}{H_d 4/3\pi a_0^3 \rho_0} = \frac{3\Sigma_d \Delta v}{\sqrt{2\pi} H_d a_0 \rho_0}, \end{aligned} \quad (\text{A15})$$

which is smaller than one in Wada et al. (2019, 2021) by a factor of 4, and the timescale of grain size growth is longer than their results by a factor of 4.

ORCID iDs

Nguyen Chau Giang  <https://orcid.org/0000-0002-3681-671X>

Thiem Hoang  <https://orcid.org/0000-0003-2017-0982>

Le Ngoc Tram  <https://orcid.org/0000-0002-6488-8227>

Nguyen Duc Dieu  <https://orcid.org/0000-0002-5678-1008>

Pham Ngoc Diep  <https://orcid.org/0000-0002-2808-0888>

Bui Van Tuan  <https://orcid.org/0000-0003-3820-1011>

Bao Truong  <https://orcid.org/0000-0001-9654-8051>

References

Alonso-Herrero, A., Esquej, P., Roche, P. F., et al. 2016, *MNRAS*, 455, 563
 Antonucci, R. 1993, *ARA&A*, 31, 473
 Barvainis, R. 1987, *ApJ*, 320, 537
 Buchner, J., Brightman, M., Baloković, M., et al. 2021, *A&A*, 651, A58
 Buchner, J., Georgakakis, A., Nandra, K., et al. 2015, *ApJ*, 802, 89
 Burke, J. R., & Silk, J. 1974, *ApJ*, 190, 1
 Burlon, D., Ajello, M., Greiner, J., et al. 2011, *ApJ*, 728, 58
 Chiang, E., Youdin, A. N., & Youdin, A. N. 2010, *AREPS*, 38, 493
 Chokshi, A., Tielens, A. G. G. M., & Hollenbach, D. 1993, *ApJ*, 407, 806
 Dominik, C., & Tielens, A. G. G. M. 1997, *ApJ*, 480, 647
 Draine, B. T. 2011, *Physics of the Interstellar and Intergalactic Medium* (Princeton, NJ: Princeton Univ. Press)
 Draine, B. T., Draine, B. T., Flatau, P. J., & Flatau, P. J. 1994, *JOSAA*, 11, 1491

Draine, B. T., & Li, A. 2007, *ApJ*, 657, 810
 Draine, B. T., & Salpeter, E. E. 1979, *ApJ*, 231, 77
 Draine, B. T., & Weingartner, J. C. 1996, *ApJ*, 470, 551
 Dullemond, C. P., & van Bemmell, I. M. 2005, *A&A*, 436, 47
 Fritz, J., Franceschini, A., & Hatziminaoglou, E. 2006, *MNRAS*, 366, 767
 Giang, N. C., & Hoang, T. 2021, *ApJ*, 922, 47
 Goldreich, P., & Ward, W. R. 1973, *ApJ*, 183, 1051
 Granato, G. L., & Danese, L. 1994, *MNRAS*, 268, 235
 Granato, G. L., Danese, L., & Franceschini, A. 1997, *ApJ*, 486, 147
 Greenberg, J. M., Mizutani, H., & Yamamoto, T. 1995, *A&A*, 295, L35
 Gundlach, B., Kiliyas, S., Beitz, E., & Blum, J. 2011, *Icar*, 214, 717
 Hao, L., Weedman, D. W., Spoon, H. W. W., et al. 2007, *ApJL*, 655, L77
 Herranen, J., Lazarian, A., & Hoang, T. 2021, *ApJ*, 913, 63
 Hicks, E. K. S., Davies, R. I., Malkan, M. A., et al. 2009, *ApJ*, 696, 448
 Hoang, T. 2019, *ApJ*, 876, 13
 Hoang, T. 2020, *Galax*, 8, 52
 Hoang, T. 2021, *ApJ*, 921, 21
 Hoang, T., Giang, N. C., & Tram, L. N. 2020, *ApJ*, 895, 16
 Hoang, T., & Lazarian, A. 2008, *MNRAS*, 388, 117
 Hoang, T., & Lazarian, A. 2014, *MNRAS*, 438, 680
 Hoang, T., & Lazarian, A. 2016, *ApJ*, 831, 159
 Hoang, T., Lazarian, A., & Martin, P. G. 2013, *ApJ*, 779, 152
 Hoang, T., & Tram, L. N. 2020, *ApJ*, 891, 38
 Hoang, T., Tram, L. N., Lee, H., & Ahn, S.-H. 2019b, *NatAs*, 3, 766
 Hoang, T., & Tung, N.-D. 2019, *ApJ*, 885, 125
 Hönig, S. F., Beckert, T., Ohnaka, K., & Weigelt, G. 2006, *A&A*, 452, 459
 Hönig, S. F., & Kishimoto, M. 2010, *A&A*, 523, A27
 Izumi, T., Wada, K., Fukushige, R., Hamamura, S., & Kohno, K. 2018, *ApJ*, 867, 48
 Kataoka, A., Tanaka, H., Okuzumi, S., & Wada, K. 2013, *A&A*, 557, L4
 Kimura, H., Wada, K., Yoshida, F., et al. 2020, *MNRAS*, 496, 1667
 Kokubo, E., & Ida, S. 2012, *PTEP*, 2012, 01A308
 Krolik, J. H., & Begelman, M. C. 1988, *ApJ*, 329, 702
 Laor, A., & Draine, B. T. 1993, *ApJ*, 402, 441
 Lazarian, A., & Hoang, T. 2007, *MNRAS*, 378, 910
 Lazarian, A., & Hoang, T. 2021, *ApJ*, 908, 12
 Li, A., & Draine, B. T. 2001, *ApJ*, 554, 778
 Li, A., & Greenberg, J. M. 1997, *A&A*, 323, 566
 Lee, H., Hoang, T., Le, N., & Cho, J. 2020, *ApJ*, 896, 44
 Litwin, K. L., Zygielbaum, B. R., Polito, P. J., Sklar, L. S., & Collins, G. C. 2012, *JGRE*, 117, E08013
 Markowitz, A. G., Krumpe, M., & Nikutta, R. 2014, *MNRAS*, 439, 1403
 Mathis, J. S., Mezger, P. G., & Panagia, N. 1983, *A&A*, 500, 259
 Mathis, J. S., Rumpl, W., & Nordisack, K. H. 1977, *ApJ*, 217, 425
 Mukai, T., Ishimoto, H., Kozasa, T., Blum, J., & Greenberg, J. M. 1992, *A&A*, 262, 315
 Nenkova, M., Ivezić, Ž., & Elitzur, M. 2002, *ApJL*, 570, L9
 Nenkova, M., Sirocky, M. M., Ivezić, Ž., & Elitzur, M. 2008a, *ApJ*, 685, 147
 Nenkova, M., Sirocky, M. M., Nikutta, R., Ivezić, Ž., & Elitzur, M. 2008b, *ApJ*, 685, 160
 Netzer, H. 2015, *ARA&A*, 53, 365
 Okuzumi, S., Tanaka, H., & aki Sakagami, M. 2009, *ApJ*, 707, 1247
 Okuzumi, S., Tanaka, H., Kobayashi, H., & Wada, K. 2012, *ApJ*, 752, 106
 Schartmann, M., Meisenheimer, K., Camenzind, M., et al. 2008, *A&A*, 482, 67
 Schartmann, M., Wada, K., Prieto, M. A., Burkert, A., & Tristram, K. R. W. 2014, *MNRAS*, 445, 3878
 Shakura, N. I., & Sunyaev, R. A. 1973, *A&A*, 500, 33
 Shen, Y., Draine, B. T., & Johnson, E. T. 2008, *ApJ*, 689, 260
 Shi, Y., Rieke, G. H., Hines, D. C., et al. 2006, *ApJ*, 653, 127
 Siebenmorgen, R., Haas, M., Krügel, E., & Schulz, B. 2005, *A&A*, 436, L5
 Stalewski, M., Fritz, J., Baes, M., Nakos, T., & Popović, L. Č. 2012, *MNRAS*, 420, 2756
 Suyama, T., Wada, K., Tanaka, H., & Okuzumi, S. 2012, *ApJ*, 753, 115
 Tatsuuma, M., Kataoka, A., & Tanaka, H. 2019, *ApJ*, 874, 159
 Tazaki, R., Ichikawa, K., & Kokubo, M. 2020, *ApJ*, 892, 84
 Tristram, K. R. W., Raban, D., Meisenheimer, K., et al. 2009, *A&A*, 502, 67
 Tung, N.-D., & Hoang, T. 2020, *ApJ*, 901, 6
 Urry, C. M., & Padovani, P. 1995, *PASP*, 107, 803
 Wada, K., Papadopoulos, P. P., & Spaans, M. 2009, *ApJ*, 702, 63
 Wada, K., Schartmann, M., & Meijerink, R. 2016, *ApJL*, 828, L19
 Wada, K., Schartmann, M., & Meijerink, R. 2016, *ApJ*, 828, L19
 Wada, K., Tanaka, H., Suyama, T., Kimura, H., & Yamamoto, T. 2008, *ApJ*, 677, 1296
 Wada, K., Tsukamoto, Y., & Kokubo, E. 2019, *ApJ*, 886, 107
 Wada, K., Tsukamoto, Y., & Kokubo, E. 2021, *ApJ*, 909, 96
 Weingartner, J. C., & Draine, B. T. 2001, *ApJ*, 548, 296
 Work, A., & Lian, Y. 2018, *PrA&S*, 98, 1